REVIEW ARTICLE

Experimental modelling of single-particle dynamic processes in crystallization by controlled colloidal assembly

Tian Hui Zhang[b] and Xiang Yang Liu*[ac]

In the last few decades, the controlled colloidal assembly was adopted as a new modelling technology for the study of the crystallization mechanism. In colloidal systems, the movement of particles is slow enough to follow and the particle dynamics can be monitored at the single-particle level using normal optical microscopes. So far, the studies of colloidal crystallization have produced a number of insights, which have significantly improved our understanding of crystallization. In this review, we summarize the recent advances in understanding the mechanism of crystallization, which were achieved using colloidal model systems, *i.e.*, the kinetics of nucleation, growth and defect formation. Such model systems allow us to not only visualize some "atomic" details of nucleation and surface processes of crystallization, but also quantify previous models to such an extent that has never been achieved before by other approaches. In the case of nucleation, the quantitative observation of the kinetic process was made at the single-particle level; the results include the ideal case and the deviations from classical theories. The deviations include multi-step crystallization, supersaturation-driven structural mismatch nucleation, defect creation and migration kinetics, surface roughening, *etc.* It can be foreseen that this approach will become a powerful tool to study the fundamental process of crystallization and other phase transitions.

[a] *Research Institute for Biomimetics and Soft Matter, Xiamen University, 422 Si Ming Nan Road, 361005 Xiamen, P. R. China. E-mail: liuxy@xmu.edu.cn; Fax: +86 592 2182775; Tel: +86 0512 69155695*

[b] *Center for Soft Condensed Matter Physics and Interdisciplinary Research, Soochow University, Suzhou, 215006, China*

[c] *Department of Physics and Department of Chemistry, National University of Singapore, Singapore 117542. E-mail: phyliuxy@nus.edu.sg*

1. Introduction

Crystallization is the process of forming solid crystals from a supersaturated solution or melt. In many cases, high quality crystals free of defects are required and, therefore, control on crystallization processes is critical. In this regard, a full understanding of the crystallization mechanism is a prerequisite. However, the current understanding of crystallization is still far from being complete although crystallization as a fundamental process in chemistry and physics has been studied intensively for more than one century. The main challenge lies in the fact that atoms in typical atomic systems are too small and move too fast for direct observation such that the dynamic processes of crystallization are not accessible to traditional visualization techniques. As alternative approaches, computer simulations and colloidal experimental modelling were developed.

Computer simulation

About half a century ago, Gilmer and Bennema pioneered the study of the crystal growth kinetics by Monte Carlo (MC) simulations.[1,2] In their simulations, the dependence of growth rate on supersaturation experiences a transition from nonlinear to linear behavior at the so-called roughening temperature as predicted by theoretical models. As a breakthrough, the theoretical models were for the first time validated by computer experiments. This success greatly promoted the application of computer simulations in the fundamental study of crystallization. So far, MC simulations have been widely used in studying crystallization.[3,4] In MC simulations, real trajectories of atoms are not concerned. Instead, a new atomic configuration is generated by assigning atoms a random displacement. The new configuration will be accepted or rejected according to a criterion based on the Boltzmann statistics.[5,6] The possible configurations can be explored by inputting random displacement through all particles in the system and continuing till an equilibrium state is reached. By MC simulations, high configuration energy barriers can be crossed over directly with the random virtual moves and, therefore, the simulation processes toward equilibrium states are greatly accelerated. In MC simulations, however, the information concerning the dynamical evolution of crystal nuclei and crystal surfaces is missing. This information

is critical in establishing the correlation between atomic processes and the end product, and therefore is a prerequisite for applying precise control on crystal growth. In this case, molecular dynamic (MD) simulation is useful. In MD simulations,[7] the trajectories of all individual atoms in a studied system are calculated by performing numerical integration of Newton's equations of motion. With the information of trajectories, the dynamical evolution of the system can be investigated at the atomic level. It is by MD simulation that the dynamical evolution of the shape and size of ice nuclei was revealed for the first time.[8] So far, to improve the accuracy of numerical integration, a number of algorithms have been developed to solve the equations of motion.[9,10]

Results obtained from computer simulations in the last few decades have greatly expanded our knowledge about the kinetics of nucleation[11,12] and the mechanism of crystal growth.[13] However, as more computer simulation results were produced, their limitations became evident. Firstly, the typical time scale that can be approached by simulations is up to 10^{-7} s even with the modest computing resource whereas crystal nucleation times may be up to at least seconds in atomic systems.[6] Secondly, the number of degrees of freedom which can be handled by current computers ranges from a few hundred to a few million. In practice, most simulations probe only systems of a few hundred to a few thousand particles. To mimic the infinite bulk environment, periodic boundary conditions are normally imposed.[10] If the concerned phenomenon has an intrinsic long-range space correlation, the output of simulations becomes unreliable due to the interference of the artificial long-range correlation produced by periodic boundary conditions.

Finally, in both MD simulations and MC simulations, potential energy has to be calculated for all particles in every simulation cycle. To obtain accurate potential energy, the interactions between the concerned particle and all other particles have to be calculated. Nevertheless, to simplify the computations in the modelling, the interactions between particles beyond a certain distance have to be truncated, which may cause a serious consequence for long-ranged interactions.[10]

Colloidal model system

Colloidal model systems were developed in the last few decades as another approach to study crystallization. Distinct from computer simulations, colloidal systems are experimental modelling systems. A colloidal system is a multi-phase system where at least a phase is highly dispersed in the other. The dispersed particles, which can be solid, liquid or gas "particles", have a size ranging from 1 nm to 10 μm. In colloidal solutions, colloidal particles exhibit Brownian motion. Due to the small size and the light mass of colloidal particles, thermal fluctuation will be displayed as the typical behaviour in colloidal dynamic processes. As a consequence, the distribution probability of colloidal particles in a potential field follows the Boltzmann distribution $\sim \exp(-U/k_B T)$ (U is the potential energy of colloidal particles). Moreover, colloidal particles in solutions can exhibit equilibrium phases, such as gas, liquid and solid, and undergo transitions among them, being analogous to that of atomic systems.[14] Based upon these features, colloidal particles in solutions can be regarded as big 'atoms'. Compared with atoms, colloidal particles are large enough for direct observation with light microscopes and their relatively

Tian Hui Zhang

Tian Hui Zhang received his PhD degree from the National University of Singapore (Prof. Xiang Yang Liu's Lab) in 2008. After that he joined Prof. Willem K. Kegel's group as a postdoctoral researcher working on controlled colloidal self-assembly at Van't Hoff Laboratory for Physical and Colloid Chemistry, Utrecht University, The Netherlands. In 2012, he joined the Center for Soft Condensed Matter Physics and Interdisciplinary as a faculty at Soochow University in Suzhou, China. His research interests focus on colloidal self-assembly and its applications in fabricating functional devices.

Xiang Yang Liu

Prof Xiang Yang Liu received his PhD degree with the cum laude title from the Radboud University Nijmegen (Netherlands) in 1993. Prof Liu is the tenured full Professor in NUS, and currently the State Distinguished Professor of the 1000 Talents Program and Chair Prof of the Changjiang Scholars Program. His research interests include biomimetics, crystallization, soft matter, etc. He has authored numerous books, and about 200 peer-reviewed papers published in prestigious journals, like Nature, etc., with many cited in the top websites and newspapers for several times. His international stand can be substantiated by his delivery of over 90 plenary/keynote or invited talks in international conferences, organization of >20 international conferences/symposia, receipt of numerous awards, and by his position as the 5th President of the Asia Association for Crystal Growth and Crystal Technology, the councillor of the International Organization of Crystal Growth, etc.

slow movement can be tracked in real time at the single-particle level. In typical colloidal suspensions, the number of colloidal particles is large enough to exhibit macroscopic bulk properties. With these features, colloidal suspensions can be used as model systems to study the phase behavior of condensed systems. An intriguing feature of colloidal model systems is that the interactions between colloidal particles can be tailored from attractive to repulsive, from short-range to long-range, from hard to soft and from symmetric to directional. Therefore, colloidal suspensions can be used to model a rich variety of systems. So far, colloids have been widely employed in studying phase transitions including crystallization,[15–19] glass transition,[20–22] melting,[23,24] etc. The purpose of this review is to summarize the recent advances in understanding the mechanism of crystallization, which were achieved using colloidal model systems.

## 2. Controlled colloidal models

Depending on the interaction between colloidal particles, colloidal model systems exhibit a range of distinct phase diagrams.[14] Among them, the simplest system is a hard sphere model. For hard spheres, there is no long-range interaction between colloidal particles and an infinite repulsion begins to work as the center-to-center distance is exactly one diameter due to the excluded volume effect (Fig. 2a, left). In hard sphere systems, only two stable phases (fluid and solid) exist (Fig. 2b, left).[25] The phase behavior is completely determined by entropy and the volume fraction is the only parameter to concern. As hard spheres are complemented with a long-range attractive interaction (Fig. 2b, middle), the system displays gas, liquid and solid phases (Fig. 2b, middle). Nevertheless, as the effective range of the attraction is shorter than 15% of the hard core diameter (Fig. 2a, right), the gas–liquid transition vanishes and the system has only two stable phases: gas and crystal. The critical point at which gas and liquid become identical shifts to the metastable region which lies below the freezing curve (Fig. 2b, right). In the metastable region, a metastable liquid–liquid transition may occur. On the other hand, if hard-spheres are complemented with a long-range repulsion, for example Coulomb repulsion, the system can exhibit fluid and (Wigner) crystal phases. In repulsive colloids, the volume fraction for fluid–crystal transition is temperature-dependent.[26]

The interactions between colloidal particles in a variety of biological and physical systems are usually a combination of attractions and repulsions. The attractive potential may arise from depletion attractions, van der Waals attractions and dipole–dipole interactions. The repulsive potential can be electrostatic repulsion, and electric and magnetic dipole–dipole interactions. The most widely used model describing the overall interactions between colloidal particles is the well-known Deryagin–Landau–Verwey–Overbeek (DVLO) theory.[27] In DVLO theory, the overall interaction is simplified as a combination of short-range van der Waals attractions and long-range electrostatic repulsions. Fig. 2d schematically summarizes the total-energy (or potential) curves in three distinct cases. (I) At low ionic

strengths, the electrostatic interaction is strong. The interactions between colloidal particles at very short-distances are attractive while the long-range interaction between colloidal particles is dominated by repulsion. A high energy barrier is then presented for colloidal particles as they tend to aggregate at a short distance. (II) At intermediate ionic strengths, there is a so-called secondary potential minimum, and a negligibly small barrier. (III) At higher ionic strengths, there is no energy barrier and the interactions between colloidal particles are dominated by attractions. For the first case, the phase behaviour of colloids becomes intrinsic: equilibrium clusters can be formed through microphase transitions as shown in Fig. 2e.[28,29] The equilibrium clusters result from the competition between the short-range attractions and the long-range repulsions.

Colloidal particles in solutions generally acquire some residual charges on their surface. Therefore playing with the charges is a widely used strategy in controlling colloidal phase transitions.[30–37] For example, polymethylmethacrylate (PMMA) spheres dispersed in the mixture of cyclohexyl bromide (CHB) and cis-decalin become positively charged, giving rise to a long-range Coulomb repulsion between them. In this kind of systems, Wigner crystals (Fig. 3a) can be formed at high effective colloidal volume fractions. By tuning the salt concentration in the solvent, PMMA particles fluorescently labelled with different dyes may acquire opposite charges. The oppositely charged colloidal particles can form ionic binary crystals as shown in Fig. 3b.[38] As the long-range repulsion is complemented with a short-range attraction, microphase separation gives rise to microcrystalline structures (Fig. 3c).[29] In this case, crystallization at low colloidal volume fractions does not produce continuous bulk crystals but crystallites with an optimum size.[39] For charged colloidal particles, electric fields are one of the most effective means for controlling colloidal self-assembly. For example, as an electrical field is applied to the charged PMMA spheres, dipole–dipole interactions lead to chain-like structures (Fig. 3d).[40] So far, numerous efforts have been dedicated to study the behavior of colloidal assembly under electric fields. The recent advances in controlling charged colloidal particles by electric fields were summarized in recent review articles by T. Palberg,[41] A. van Blaaden[42,43] and Liu et al.[44] The application of confocal microscopes allows the direct observation of three-dimensional (3D) colloidal structures at the single-particle level as illustrated in Fig. 3. However, nucleation, the early stage of crystallization, is a dynamic process. The competing effect between resolution and scanning speed makes it a challenge to monitor a 3D nucleation process in real-time using confocal microscopes. In contrast, nucleation in two-dimensional (2D) colloidal model systems as illustrated in Fig. 1b can be followed in real-time using normal light microscopes coupled with high speed digital CCD cameras.

Fig. 4a illustrates an experimental system controlled by alternating electric field (AEF). As the AEF is applied, two-dimensional (2D) colloidal self-assembly occurs on electrodes.[17,33,37,44,45] In comparison with other stimuli, the electric stimulus can be switched on/off instantly without disturbing the original solutions after experiments. This system has been

2326 | Chem. Soc. Rev., 2014, **43**, 2324–2347

This journal is © The Royal Society of Chemistry 2014
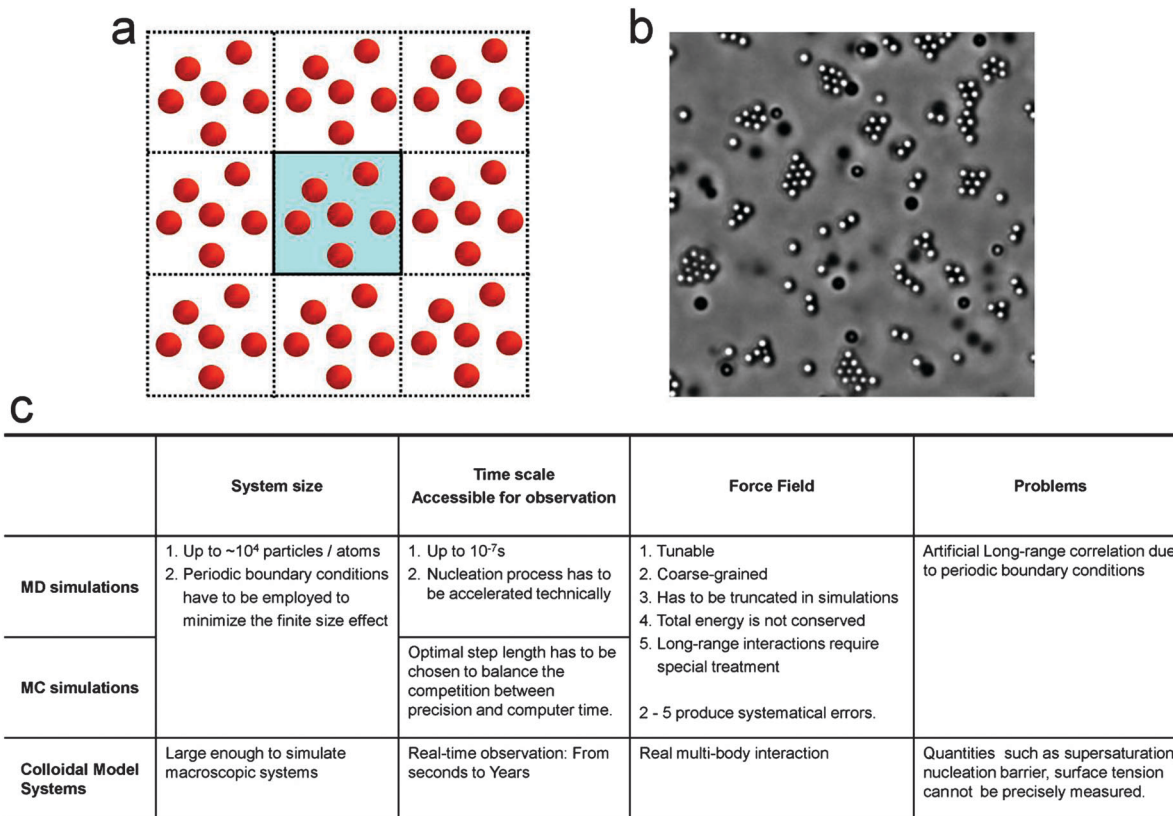
Fig. 1 (a) Schematic illustration of periodic boundary conditions in computer simulations. For a finite system with boundaries, particles near the boundaries are not surrounded by neighboring particles in all directions and thus are subjected to a non-isotropic force field. To avoid the artificial boundary effects, periodic boundary conditions are usually employed: the simulation box is periodically repeated in all directions; in simulations, when a particle leaves the central simulation box, one of its image particles enters the central box from the opposite direction. (b) A snapshot of nucleation occurring in a two-dimensional colloidal model system. There are no artificial boundary effects. (c) Characteristic list of computer simulations and colloidal model systems.

employed in studying fundamental phenomena including crystallization,[17,18] melting,[24] crystal defects[46] and the kinetics of crystal growth.[47] Since results achieved in this model system are an essential part of this review, an understanding of the mechanism controlling the colloidal assembly may make it easier for the readers to go through the related contents.

The 2D assembly of charged colloidal particles on electrodes (Fig. 4a) is driven by electrohydrodynamic (EHD) flow.[48–50] The mechanism is that the dissolved ionic species build up an electric double layer adjacent to the electrode surface, which is then disrupted by the presence of charged colloidal particles, leading to spatially varying free charge. The presence of charged colloidal particles also distorts the applied field, leading to a lateral electric field. The interaction between the free charges and the lateral electric field sets up the EHD flow. According to the studies of Ristenpart et al.,[49,51] the tangential EHD velocity along the electrode surface scales as

$$u_t \sim \frac{3\varepsilon\varepsilon_0}{\mu\kappa}E_\infty^2\left\{C_0' + \frac{D\kappa^2}{\omega}C_0''\right\} \quad (1)$$

where E_∞ is the strength of the incident electric field, ε_0 is the permittivity of free space and κ is the reciprocal Debye length. D denotes the ionic diffusion coefficient and ω is the angular frequency of the AEF. C_0' and C_0'' are parameters associated with the dipole coefficient. There is a frequency range within which the EHD velocity is negative, leading to an attractive Stokes force that causes particle assembly. Outside this frequency range the velocity becomes negligible or positive.

Except the interaction induced by the EHD flow, repulsive electrostatic Coulomb interactions and dipole–dipole interactions also play a key role in this system.[52–54] The competition between the attractive force and the repulsive force determines whether the colloidal particles aggregate or disperse. According to eqn (1), the EHD flow induced attractive force decays upon increasing the frequency. In contrast, dipolar interactions between identical particles increase with the strength of AEF by E_∞^2 and roughly remain constant at different frequencies.[49] It follows that the 2D colloidal aggregation on electrodes can occur only below a critical frequency above which the EHD flow is negligible and the repulsive dipolar interactions become dominant. Within the frequency window of aggregation, the normalized equilibrium distance r_{eq} in a 2D colloidal crystal becomes larger upon increasing the frequency at the high value side (>500 Hz), and at a higher temperature, the frequency window for 2D crystalline assembly becomes wider (Fig. 4d).[45] The mechanism is that an increase in the temperature results

This journal is © The Royal Society of Chemistry 2014

Chem. Soc. Rev., 2014, 43, 2324–2347 | 2327
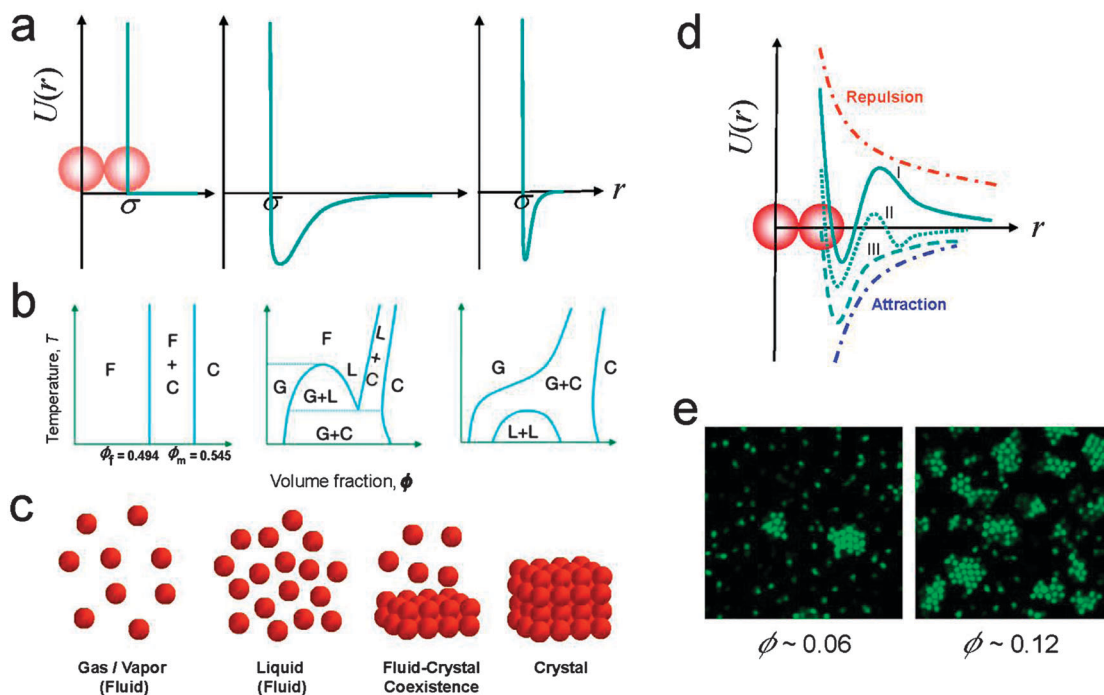
Fig. 2 Phase diagrams in colloids. (a) Interactions between colloid particles. From left to right: hard sphere interaction, long-range attraction, short-range attraction. (b) Left: in hard-sphere systems, only fluid (F) and crystal (C) phases exist. Middle: phase diagram of hard spheres with long-range attractions, an analogue of atomic systems. Right: in cases where the attraction is short-range, as in protein systems (important in physiology), equilibrium between gas (G) and crystal (C) is found, but the liquid (L)–liquid (L) transition becomes metastable. (c) Schematic representation of phases in colloids: gas, liquid, crystal. (d) Schematic representation of DVLO theory. Curves (I), (II), and (III) refer to three distinct situations upon increasing the concentration of electrolytes. (e) Equilibrium cluster phases obtained in colloids with competing short-range (depletion) attractions and long-range (electrostatic) repulsions at different volume fractions. (b) Reprinted with permission from Macmillan Publishers Ltd: Nature (ref. 14), copyright (2002). (e) Reproduced from ref. 29 with permission from The Royal Society of Chemistry.
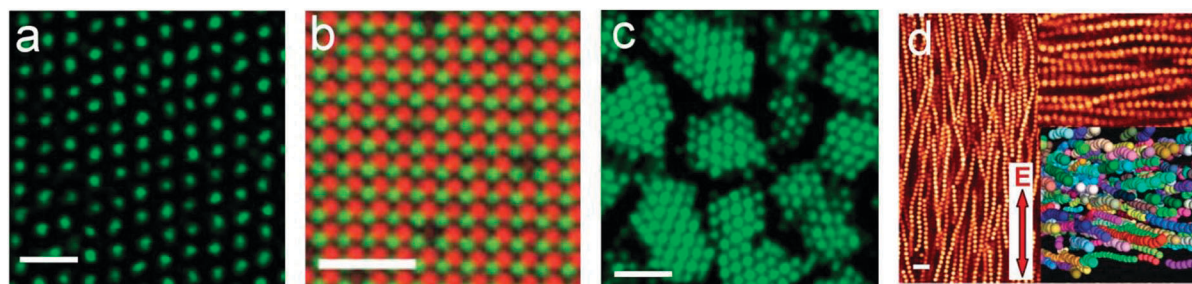

Fig. 3 Colloidal crystallization in systems characterized by different interactions. (a) Wigner crystal in long-range repulsive colloids. Scale bar: 5 μm. (b) Ionic binary crystals in systems with oppositely charged colloids. Scale bar: 10 μm. (c) Microcrystals in colloids with competing short-range attractions and long-range repulsions. Scale bar: 5 μm. (d) Chain-like structures due to dipole–dipole interactions induced by external electrical fields. Scale bar: 5 μm. (b) Reprinted with permission from Macmillan Publishers Ltd: Nature (ref. 38), copyright (2005). (d) Adapted with permission from ref. 40. Copyright (2012) WILEY-VCH Verlag GmbH & Co. KGaA, Weinheim.

in an increase in the ionic diffusion coefficient D, which according to eqn (1) tends to enhance the EHD flow induced attraction. In Fig. 4e, the equilibrium distance r_{eq} displays no significant change upon increasing the strength of the AEF, as the attraction and the dipolar repulsion are enhanced simultaneously. However, in the low frequency regions, the behavior of r_{eq} deviates from the prediction of the EHD flow mechanism. First, as the frequency is below 500 Hz, the equilibrium distance decreases upon increasing the frequency (Fig. 4d). Moreover, Fig. 4e shows that in the frequency window of 100–200 Hz, r_{eq} increases with the field strength. At a very low frequency of 40 Hz, r_{eq} can even be tuned from $1.05 \times 2a$ to $2.23 \times 2a$ (a is the diameter of colloidal particles) upon increasing the field strength (Fig. 4f).

To address the behavior of r_{eq} in the low frequency regions, electroosmotic flow (EOF) has to be taken into account. Ristenpart et al. suggested[55] that in steady electric fields, both the EOF mechanism and the EHD mechanism are responsible for the 2D aggregation on electrodes. The EOF mechanism arises from the influence of the incident steady electric field on

2328 | Chem. Soc. Rev., 2014, **43**, 2324–2347

This journal is © The Royal Society of Chemistry 2014
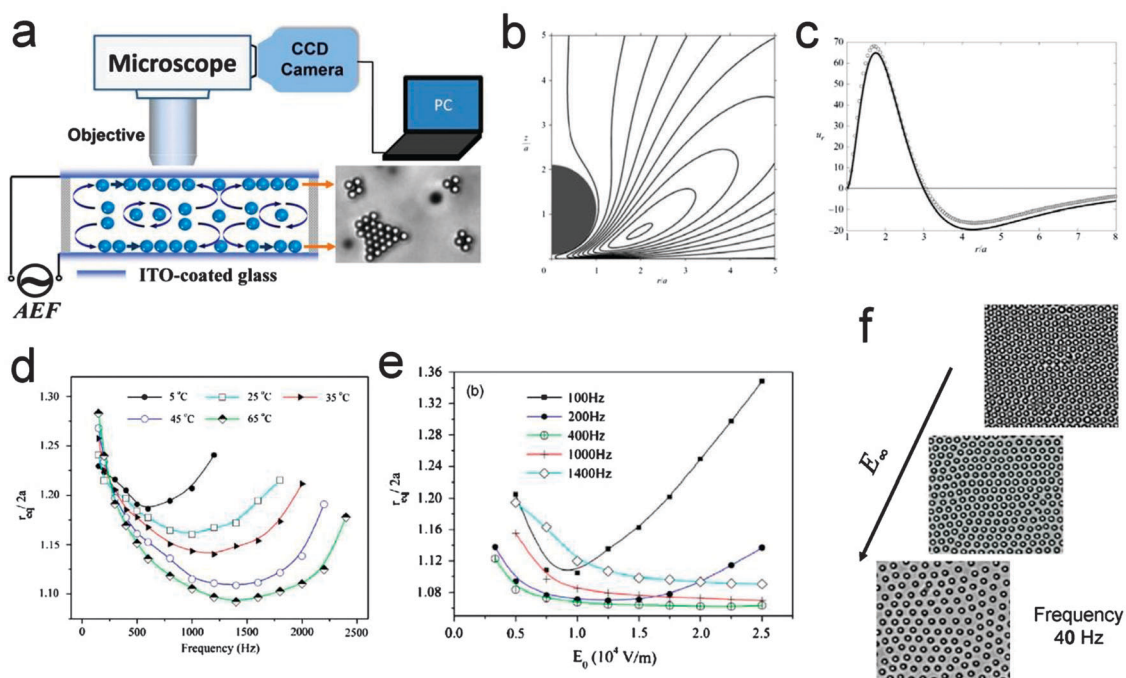
Fig. 4 AEF-induced 2D colloidal assembly. (a) The schematic of the experimental setup. The colloidal suspension is sandwiched between two ITO-coated glass plates separated by insulating spacers. The crystallization processes are recorded by a digital imaging camera which is mounted on the microscope. (b) EHD flow around colloidal particles near the electrodes. For $C_0' < 0$, the flow direction is clockwise and it is counterclockwise for $C_0' > 0$. (c) A representative plot of the radial EHD velocity u_r, around a colloid near the electrode. For negative u_r, the EHD flow brings another particle close, and *vice versa*, the flow carries another colloidal particle away. $\bigcirc$, numerical solution with a volumetric body force; $-$, analytical solution with slip conditions specified at the boundaries. (d) Variation of the dimensionless equilibrium distance $r_{eq}/2a$ with frequency at different temperatures at field strength $E_\infty = 1.5 \times 10^4$ V m^{-1}. (e) $r_{eq}/2a$ as a function of the field strength E_0 (E_∞) at different frequencies with a temperature of 25 °C. (f) Colloidal assembly at different field strengths (from top to bottom) of 5.8×10^4, 7.5×10^4, and 8.3×10^4 V m^{-1}. The measured equilibrium distance $r_{eq}/2a$ is 1.34, 1.66, and 2.23 respectively. (b and c) Adapted with permission from ref. 49. Copyright (2007) Cambridge University Press. (d–f) Adapted with permission from ref. 45. Copyright (2007) AIP Publishing LLC.

the equilibrium diffuse layers of particles. The strength of EOF, u_{EOF}, is proportional to the field strength E_∞ and the particle surface potential ζ, $u_{EOF} \sim \zeta E_\infty$. In a steady field, the EHD flow scales as $u_t \sim E_\infty \log E_\infty$. The attractive EHD flow works at a distance far from the particles while the attractive EOF becomes dominant near the particles. The EOF model is based on a steady electric field. Nevertheless, if the frequency is not higher than one thousand Hz, the EOF mechanism is still valid for an AEF. In the low frequency region, on increasing the field strength, both the EHD flow and the EOF are enhanced. Simultaneously, increasing the field strength also enhances the repulsive dipolar interaction. Since the repulsive dipolar interaction is proportional to the square of field strength,[53,54] the increase of repulsion overwhelms the increase of attraction, giving rise to a larger equilibrium separation at a stronger AEF as shown in Fig. 4f. In addition, Fig. 4d indicates that decreasing the frequency in the low frequency region will increase r_{eq}. This behaviour so far has not been well understood. It follows that at low frequencies, the mechanism underlying the 2D colloidal aggregation is complex. In experiments, colloidal crystallization was usually studied in the frequency window where the EHD mechanism is valid.

Finally, in this system, ionic concentration and particle size also play their role in determining the assembly kinetics and the boundary frequencies for 2D assembly. In practice,

adjusting ionic concentration by salts is also an important strategy in controlling the 2D assembly.

Fig. 5 presents a summary of the phase behavior of the AEF-controlled system in space of field strength E_∞ and frequency ν. The obtained structures range from oscillating vortex rings to interlinked chains and from 2D crystals to 3D assembly. Fig. 5a shows a 2D crystal obtained at $E_\infty = 2.6 \times 10^4$ V m^{-1} and $\nu = 800$ Hz. By decreasing the frequency, a disordered 3D assembly is formed at $E_\infty = 2.4 \times 10^4$ V m^{-1} and $\nu = 100$ Hz (Fig. 5b). The chain structures in Fig. 5c were observed oscillating in the frequency of the AEF. The structure of the 3D stationary assembly in Fig. 5b and c is formed by fluorescent spheres, which is visualized using a laser scanning confocal microscope (LSCM). In the vortex ring (Fig. 5d), colloidal spheres move downwards along the inner surface and move upwards along the exterior.[56] Depending on the particle size and the electrolyte concentration, the phase boundaries in Fig. 5 may shift.

3. Thermodynamic driving force for crystallization

In general, the thermodynamic driving force for crystallization is the minimization of free energy. In other words, crystallization
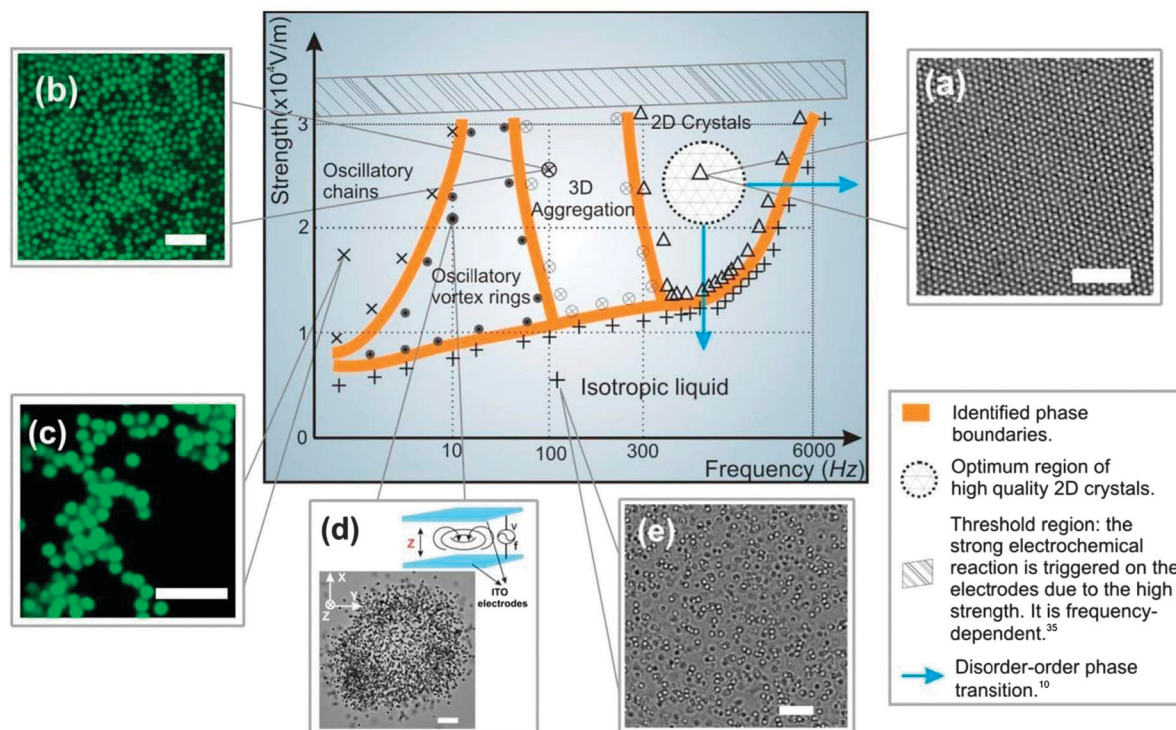
Fig. 5 The phase diagram and typical colloidal patterns induced by an AEF. (a) A 2D colloidal crystal at field strength $E_\infty = 2.6 \times 10^4$ V m^{-1} and frequency $v = 800$ Hz. (b) 3D assembly of colloidal particles, as captured by the LCSM at $E_\infty = 2.4 \times 10^4$ V m^{-1} and frequency $v = 100$ Hz. (c) Static snapshot of colloidal chains by the LCSM at $E_\infty = 1.8 \times 10^4$ V m^{-1} and frequency $v = 0.1$ Hz. (d) Snapshot of oscillatory vortex rings at $E_\infty = 2.3 \times 10^4$ V m^{-1} and frequency $v = 1$ Hz. (e) The isotropic liquid state of colloidal suspension. Scale bars: 5 μm in (b) and (c); 10 μm in (a), (d) and (e). Reprinted with permission from ref. 56. Copyright (2009) AIP Publishing LLC.

occurs because the chemical potential μ_i^{ambient} of a growth unit in the ambient mother phase is higher than the chemical potential μ_{crystal} in a crystal phase. The difference between the chemical potentials μ_i^{ambient} and μ_{crystal} is given by

$$\Delta\mu = \mu_i^{\text{ambient}} - \mu_{\text{crystal}} \tag{2}$$

(The subscript i denotes the solute in the ambient phase.) In solutions, the chemical potential of species i is given by[57,58]

$$\mu_i = \mu_i^0 + k_B T \ln a_i \approx \mu_i^0 + kT_B \ln C_i \tag{3}$$

where a_i denotes the activity of species i which is often approximated by concentration C_i. μ_i^0 denotes the chemical potential of species i in a standard state ($a_i = 1$). With eqn (3), the thermodynamic driving force for crystallization is given by

$$\frac{\Delta\mu}{k_B T} = \ln\frac{a_i}{a_i^{\text{eq}}} \approx \ln\frac{C_i}{C_i^{\text{eq}}}, \tag{4}$$

(a_i^{eq} and C_i^{eq} are, respectively, the equilibrium activity and concentration of species i.) Given the definition of the supersaturation σ for crystallization

$$\sigma = (a_i - a_i^{\text{eq}})/a_i^{\text{eq}} \approx (C_i - C_i^{\text{eq}})/C_i^{\text{eq}} \tag{5}$$

Eqn (4) can be simplified as

$$\Delta\mu/k_B T = \ln(1 + \sigma) \cong \sigma \text{ (in the case of } \sigma \ll 1) \tag{6}$$

In the case of $\Delta\mu > 0$, the system is said to be supersaturated and nucleation and crystal growth are thermodynamically expected. Conversely, when $\Delta\mu < 0$, the system is undersaturated and crystals will dissolve. For $\Delta\mu = 0$, the ambient phase is in equilibrium with the crystalline phase. As a general rule, eqn (6) can be applied to crystallization in colloidal systems as well.

4. Nucleation

Nucleation is the first stage of crystallization. By nucleation, the initial embryos of crystals are formed from a supersaturated mother phase. Whether crystal phases can occur or not and the quality of final crystals, to a large extent, are determined by nucleation processes. Therefore, applying control on nucleation processes is critical for applications requiring high quality crystals. To apply precise control on nucleation processes, a complete understanding of nucleation is necessary. Currently, the most widely used theory about nucleation is the so-called classic nucleation theory (CNT) which was initially developed about 80 years ago.[59–61] Based on CNT, nucleation processes can be well quantified by qualities such as nucleation barrier and nucleation rate.

4.1 Classical nucleation theory

In a supersaturated liquid, the growth unit in the metastable liquid phase has a higher chemical potential than that in a bulk crystal. By transferring a growth unit from the metastable liquid phase

to the bulk crystal phase, the free energy of the system is lowered by $\Delta\mu$ as eqn (2) indicates. However, the crystal surface is a different matter. Compared with the bulk units, the growth units on the surface are weakly bound to their neighbours. The free energy difference between a bulk unit and a surface unit gives rise to the surface free energy or surface tension. Due to the surface tension, the formation of a surface contributes a positive addition to the overall free energy. The free energy change associated with the formation of a crystalline nucleus is the sum of decreasing bulk free energy and increasing surface free energy, namely,

$$\Delta G = -n\Delta\mu + \Phi_n \qquad (7)$$

where n is the size of the nucleus (number of growth units in the nucleus) and Φ_n is the total surface energy of the n-sized nucleus. For spherical nuclei with a radius R, one has $n = 4\pi R^3\rho_c/3$ and $\Phi_n = 4\pi R^2\gamma$ and eqn (7) can be expressed as

$$\Delta G = -\frac{4\pi}{3}R^3\rho_c\Delta\mu + 4\pi R^2\gamma \qquad (8)$$

where ρ_c is the particle number density of nuclei and γ is the surface free energy area density. From eqn (8), it is clear that nucleation is a process controlled by the competition between the decreasing bulk free energy and the increasing surface free energy. As a consequence of the competition, ΔG experiences a maximum ΔG^* at $R = R_c$ (Fig. 6a). Mathematically, ΔG^* and R_c are defined by $0 = \mathrm{d}(\Delta G)/\mathrm{d}R$. The results are represented by eqn (9).

$$\Delta G^* = \frac{16\pi\gamma^3}{3(\rho_c\Delta\mu)^2} \text{ and } R_c = \frac{2\gamma}{\rho_c\Delta\mu} \qquad (9)$$
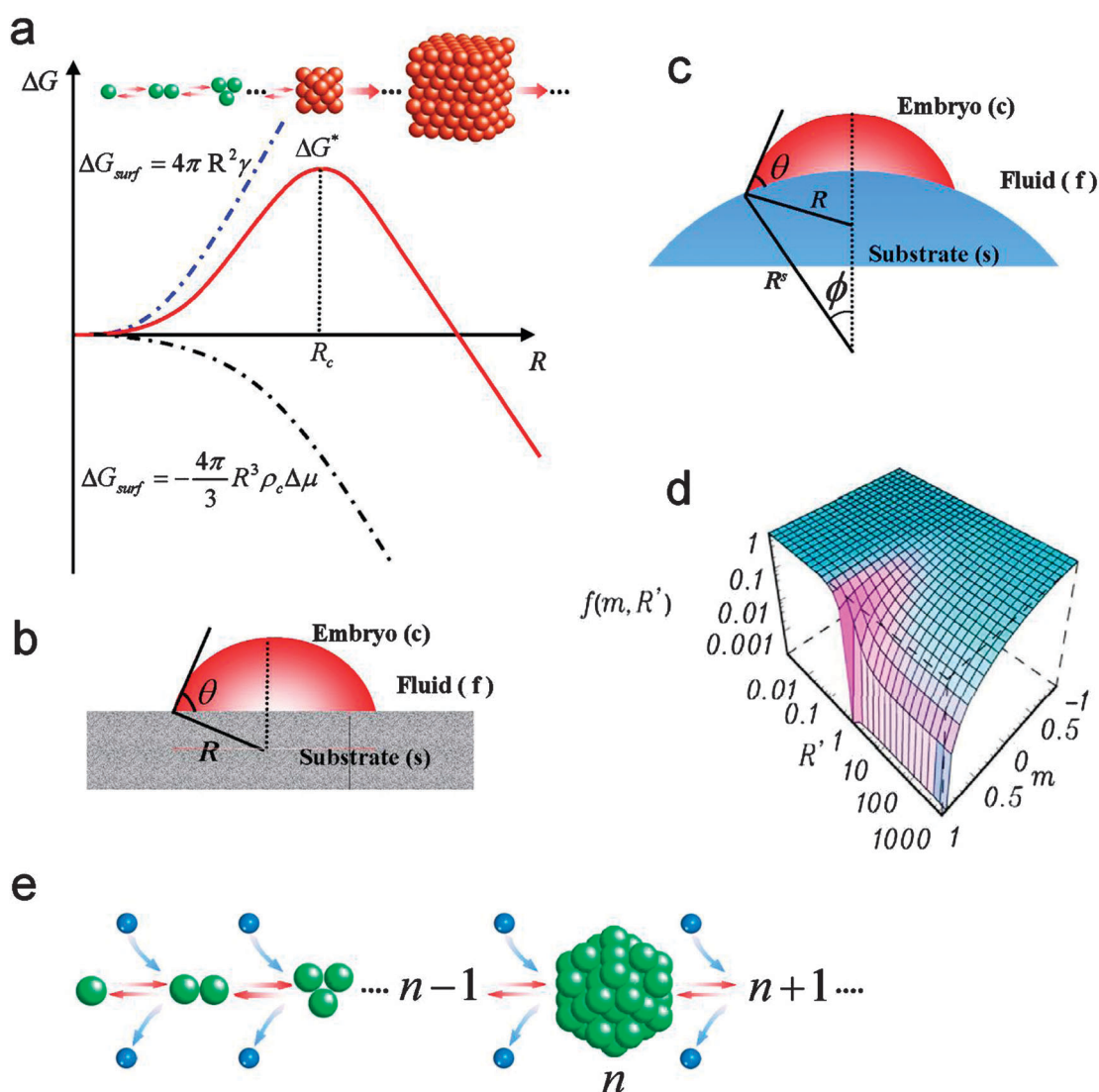
Fig. 6 Classical nucleation theory. (a) Nucleation barrier. Nuclei have to reach a critical size before they become thermodynamically stable. (b) Heterogeneous nucleation on a flat substrate. Nucleation preferentially occurs on substrates due to the reduced nucleation barrier. (c) Heterogeneous nucleation on a curved substrate. (d) Interfacial correlation factor $f(m,R')$ as a function of R' and m. (e) Classical scenario of growth of nuclei. During the growth, only one monomer is incorporated at a time. Green sphere: growth units belong to a growing cluster; blue sphere: free growth units.

$\Delta G^\star$ and R_c are the so-called nucleation barrier and the critical size respectively. The nucleation barrier has to be overcome to form a stable crystal phase. In other words, crystal nuclei have to reach the critical size R_c before they become thermodynamically stable. For sub-critical nuclei, the positive surface free energy is dominant because most of the growth units reside at the surface. Therefore, sub-critical nuclei have to be created by fluctuation.

Eqn (7)–(9) represent the results for 3D nucleation. During crystal growth, the so-called 2D nucleation often takes place at crystal surfaces. Although 3D and 2D nucleation are not exactly the same, there are a number of theoretical treatments and experimental observations showing that they share many common features in almost all aspects, such as the existence of nucleation barrier and critical size for nuclei;[62–65] the analysis on 2D nucleation can be applied to 3D nucleation, and vice versa.[66,67] For example, the mechanism of multi-step crystallization observed in 2D colloidal systems is well followed by 3D nucleation.[68–70] For 2D nucleation, the nucleation barrier and the critical size are given by

$$\Delta G^*_{2D} = \frac{\pi\gamma^2}{\rho_c\Delta\mu} \text{ and } R_c^{2D} = \frac{\gamma}{\rho_c\Delta\mu} \quad (10)$$

Nucleation on foreign bodies. Eqn (9) is based on the assumption that the probability of forming a critical nucleus is uniform throughout the system, the so-called homogeneous nucleation. However, nucleation is often promoted by the presence of foreign bodies, such as the wall of solution containers, foreign particles or substrates (Fig. 6b). The occurrence of a foreign body will normally lower the interfacial (or surface) free energy and thus reduce the nucleation barrier. Therefore, nucleation prefers to occur near or on the foreign bodies, which is known as heterogeneous nucleation. The effect of foreign bodies in lowering the nucleation barrier can be quantified by an interfacial correlation factor $f(m)$ which is defined as[66,71]

$$f(m) = \Delta G^*_{hetero}/\Delta G^*_{homo} \quad (11)$$

where ΔG^*_{homo} is the homogeneous nucleation barrier as defined by eqn (9) and ΔG^*_{hetero} is the heterogeneous nucleation barrier. $f(m)$ indicates how much the nucleation barrier is reduced with respect to ΔG^*_{homo} due to the occurrence of foreign bodies/substrates. The parameter m describes the structural match between the nucleating phase and the substrate. For a flat substrate (Fig. 6b), one has[71]
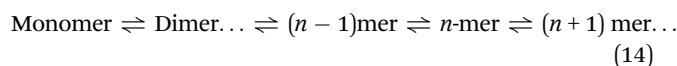
$$f(m) = \tfrac{1}{4}(2 - 3m + m^3) \quad (12)$$

with

$$m = (\gamma_{sf} - \gamma_{sc})/\gamma_{cf} \approx \cos\theta \quad (-1 \leq m \leq 1) \quad (13)$$

where θ is the contact angle of the nucleus on the substrate, and γ_{sf} and γ_{sc} are the surface free energy between the substrate and the fluid phase, and the substrate and the crystal phase, respectively. In the case of a perfect match, $\gamma_{sc} \to 0$ and $m \to \gamma_{sf}/\gamma_{cf}$. In the case of $\gamma_{sf} \approx \gamma_{cf}$, $m \to 1$ and $f(m) \to 0$. This implies that the heterogeneous nucleation barrier vanishes almost completely. This occurs when the new layer of crystal is well ordered and oriented with respect to the structure of the substrate. As the structural match changes from a perfect match to a poor match, m decreases from 1 to -1. When $m \to -1$ ($f(m) \to 1$), there is no correlation between the substrate and the nucleating phase. In this case, the substrate exerts almost no influence on nucleation, which is equivalent to homogeneous nucleation. Nuclei emerging in this case are completely disordered, bearing no correlation to the substrate. In general, for a certain system, m is between -1 and 1, which means the primary nucleation is normally governed by heterogeneous nucleation. Apart from the interfacial parameter m, the interfacial correlation factor $f(m)$ is also a function of the radius of the *relative* curvature of substrates $R' = R^s/R_c$ (R^s: the radius of the curvature of substrates) (Fig. 6c). Fig. 6d shows that interfacial correlation factor $f(m,R')$ as a function of R' and m. Notice that R_c is a function of supersaturation, and so is $f(m,R')$.

Nucleation kinetics. The widely accepted kinetic model of nucleation (within the cluster approach) was used first by Farkas in 1927.[72] It is based on the Szilard scheme of successive "chain reaction" between monomer molecules and n-sized clusters:

$$\text{Monomer} \rightleftharpoons \text{Dimer}\ldots \rightleftharpoons (n-1)\text{mer} \rightleftharpoons n\text{-mer} \rightleftharpoons (n+1)\text{ mer}\ldots \quad (14)$$

In the "chain reaction", nuclei grow by incorporating one monomer at a time (Fig. 6e). Regarding the nucleation process, there exist three physically distinct states which are of particular interest: the equilibrium, the stationary (or steady) and the nonstationary states. In the following, we will briefly discuss the equilibrium and the nonstationary states and concentrate more on the steady state.

(1) Equilibrium state. This state assumes that the cluster size distribution follows the equilibrium cluster size distribution or the Boltzmann law. As nucleation is a non-equilibrium state, the equilibrium state is just a reference state which never exists.

(2) Stationary (or steady) state. The stationary state is one of the most relevant states, which corresponds to the state where the cluster size distribution does not change with time. This is a state which occurs only in a certain period of nucleation processes.

Taking into account the effect of substrates on both the nucleation barrier and the transport process, and the fact that the average nucleation rate in the fluid phase depends on the density and size of the foreign particles present in the system, the nucleation rate is given by[71,73,74]

$$J = f''(m)[f(m)]^{1/2} \times B\exp\left[-\frac{16\pi\gamma_{cf}^3\Omega^2}{3kT[kT\ln(1+\sigma)]^2}f(m)\right] \quad (15)$$

and

$$f''(m) = \tfrac{1}{2}(1 - m) \quad (16)$$

where B is the kinetic constant. In homogeneous nucleation, the growth units can be incorporated into the nuclei from all

directions. However, in heterogeneous nucleation, the growth units from the side of the substrate are blocked from colliding with the surface of nuclei. This is comparable to a "shadow" cast on the surface of nuclei.[66,75] The "shadow" effect of substrates is described by $f''(m)$ in the pre-exponential factor, which is the ratio between the average effective collision in the presence of substrates and that of homogeneous nucleation (*i.e.*, in the absence of a substrate).

Note that for homogeneous nucleation, one has $f''(m) = f(m) = 1$. In this case, eqn (16) is converted to

$$J = B \exp\left[-\frac{16\pi\gamma_{cf}^{3}\Omega^{2}}{3kT[kT\ln(1+\sigma)]^{2}}\right] \quad (17)$$

Similar to 3D nucleation, the 2D nucleation rate J^{2D} adopts the form[66]

$$J^{2D} = C\frac{2D_s n_1^2}{\pi}\exp\left[-\frac{\pi\Omega\gamma_{step}^{2}}{(kT)^2\ln(1+\sigma)}\right] \quad (18)$$

where C is the kinetic coefficient, D_s is the diffusion coefficient, n_1 is the number of nucleating molecules (monomer), and γ_{step} is the step free energy.

(3) *Non-stationary (or non-steady) state.* There is a sequence of transient states, the so-called non-stationary state, before nucleation reaches the steady state and crystallization approaches the end. When nucleation is non-stationary, the nucleation rate is time-dependent and this non-stationary nucleation rate $J_{nonst}(t)$ changes with time.

4.2 Experimental modelling to verify classical nucleation theory

Eqn (9)–(18) have been widely used in analyzing observations of nucleation for a long time. However, experimental verification in particular the direct measurement of the distribution of sub-critical nuclei had never been achieved till a controlled 2D colloidal nucleation was carried out recently by Liu *et al.*[37] This study was conducted in the 2D colloidal model system (see Fig. 4a). In their study, the size distribution of 2D sub-critical nuclei was measured such that the scenario of CNT can be quantitatively examined. Fig. 7a presents a typical size distribution of nuclei obtained at different times. Upon supersaturating the system with the AEF, small nuclei form. Subsequently as the size of nuclei exceeds a critical value, nuclei gradually grow into crystallites. The size beyond which the profile of distribution becomes steady (Fig. 7a, inset) is defined as the transient size $n^*(t)$ at time t. The nucleation starts from a non-stationary state ($t = 3.2$ s) and gradually approaches a stationary state ($t > 20$ s) in which the distribution of nucleating clusters Z_n becomes independent of time. Once the distribution of nucleating clusters becomes steady, the nucleation event is regarded successful. The cluster size measured at $Z_{n^*}(t) = 1$ is then taken as the critical size of nucleation n_c at time t. It is found that n_c is time-dependent and only after the stationary state, the transient size n_c can acquire a constant value (Fig. 7b). It follows that the critical size of the nucleus is well-defined only at a stationary state. To determine the nucleation rate (the average number of newly formed supernuclei per unit time in a unit area), the number of supercritical nuclei was counted as a function of time. The slope of the linear fitting gives the nucleation rate (Fig. 7c). In this study, the nucleation rate as a function of the driving force σ is well described by a linear behaviour of $\ln(J) \sim 1/\ln(1 + \sigma)$, suggesting that eqn (18) is qualitatively valid in describing 2D nucleation processes.

4.3 CNT and its limitation

The results presented in Fig. 7 demonstrate that CNT is in principle valid as long as the condition of the steady state is applied and the actual nucleation condition does not deviate further from the presumptions listed below:[65]

1. The interior structures and densities of nuclei are uniform and identical to an infinite bulk crystal (in the case of crystallization). Consequently, the properties of nuclei can be characterized by only one parameter, the size of nuclei. In the system, local density is the only order parameter to distinguish the old phase and the new phase.

2. The surface free energy of crystal nuclei is the same as that of bulk crystals and is independent of the size of nuclei.

3. Nuclei grow by incorporating one monomer at a time and the incorporation of clusters is neglected.

4. The stationary distribution of sub-critical nuclei holds.

Based on these presumptions, a nucleation process is simplified, so that it can be quantified with reasonable precision. However, there are a number of discrepancies between the predictions of CNT and the actual observations. For example, the nucleation rates derived from CNT were found to be 1–10 orders of magnitude higher than experimentally measured rates,[76,77] and experimentally, the nucleation rate reaches a maximum upon increasing supersaturation.[78–81] There are also some discrepancies between the experimentally observed and the predicted kinetic factors.[82,83] The discrepancies suggest that CNT has its intrinsic limitations (Fig. 8).

5. Non-classical nucleation routes

The deviations from CNT are attributed to various reasons. The presumptions of CNT about the structure of nuclei identical to the structure of the bulk phase may be one of the main causes. For example, in the study by Kawasaki and Tanaka,[84] the formation of crystal nuclei is mediated by a transient intermediate ordered phase. This is in contrast to the assumptions by CNT. Since the properties of nuclei are of great importance for nucleation processes, direct experimental visualization of the structure and shape of nuclei is critical in advancing our understating of nucleation.

Nonspherical nuclei

A direct experimental observation of crystal nuclei was made by Gasser *et al.*[16] in a colloidal system using confocal microscopy. This allows a direct observation of nuclei in real-space. It was found that the nuclei exhibit an elliptical shape (Fig. 9a).
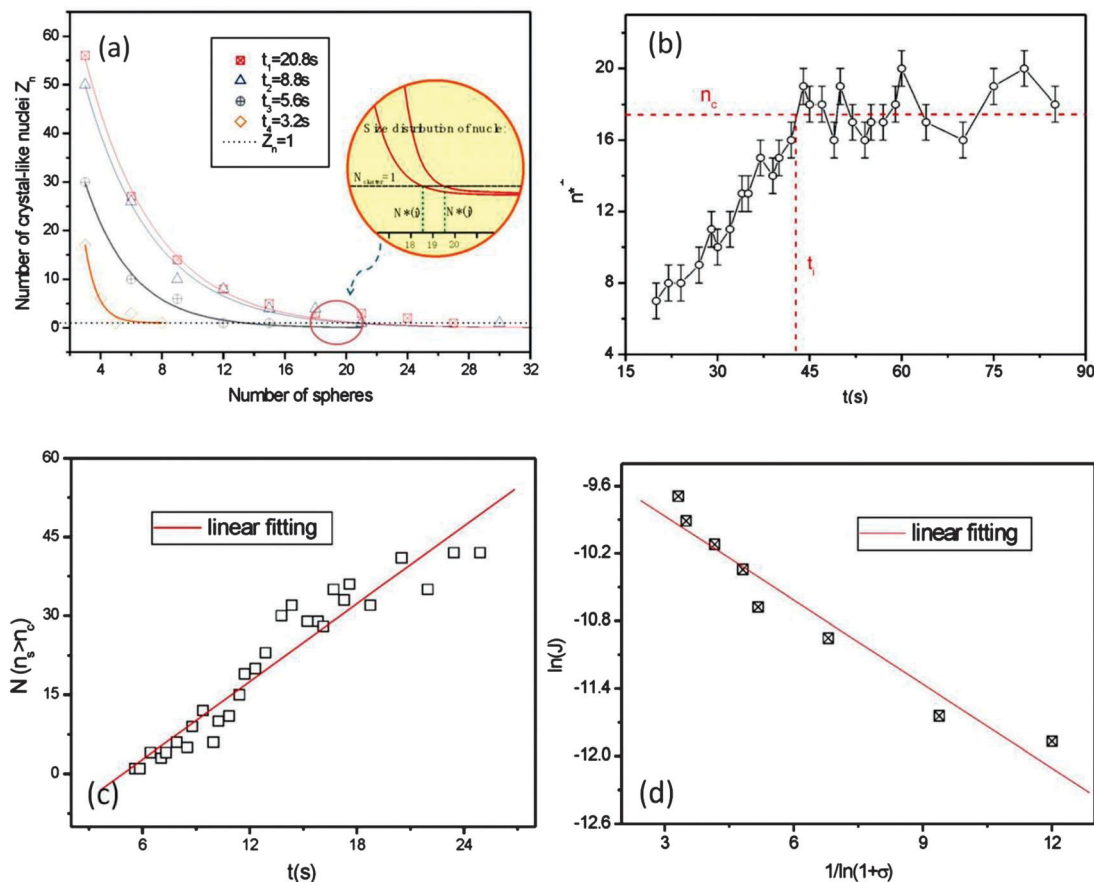
Fig. 7 Statistical measurement of nucleation kinetics. (a) The typical size distribution of sub-critical nuclei *versus* time (E_∞ = 2.6 $\times$ 10^4 V m^{-1} and v = 600 Hz). (b) $n^*(t)$ *versus* time. After the induction time, $n^*(t)$ becomes stable. The critical size can be determined. (c) The number of nuclei larger than the critical size as a function of time. The nucleation rate is defined by the slope of the linear fitting. (d) The nucleation rate under different supersaturations (driving force). The straight fitting is based on eqn (18). From eqn (18), the line tension can be determined. The value of γ_{step} is 0.50 kT/a (a is the diameter of colloidal particles) which is in agreement with the measurements. Reprinted with permission from Macmillan Publishers Ltd: Nature (ref. 37), copyright (2004).

Nonspherical nuclei were also found in protein systems. As a type of colloidal particles, globular proteins exhibit a similar phase behavior.[12,85] Therefore, the studies of protein crystallization in the last few decades also provide insight into the properties of nuclei. In apoferritin protein solutions, planar nuclei were observed by Yau *et al.* using an atomic force microscope.[86] The observation of nonspherical nuclei offers an interpretation of the failure of CNT. In CNT, the nucleation rate is determined substantially by the nucleation barrier as eqn (17) and (18) indicate. Since the prediction of nucleation barrier of CNT is based on spherical nuclei, the nucleation barrier and thus the nucleation rate of nonspherical nuclei cannot be described by CNT. One plausible understanding of the nonspherical nuclei is that nonspherical shape and their rough surface offer more attachment sites for incoming particles, promising a faster kinetics of nucleation.[87] In addition to the kinetic cause, the interactions between colloidal particles also play a critical role in determining the structure and the shape of nuclei. For example, in colloids with competing short-range attractions and long-range repulsions, experimental observations found linear structures which thermodynamically

promise a lower free energy and an easier pathway for nucleation.[29,88] From these observations, it follows that nucleation processes in many cases are complicated by kinetic causes which in CNT are taken into account.

Size-dependent structure of nuclei

While the shape of nuclei is an important parameter in nucleation, the structure of nuclei is another critical parameter. In CNT, the structure of crystal nuclei is assumed to be identical to that of bulk crystals. However, by MD and MC simulations, ten Wolde *et al.* found that the structure of nuclei may be size-dependent.[89] If this prediction is true, CNT has to be revised. To verify this prediction, direct experimental observation is essential. In this case, 2D nucleation in colloids promises a better experimental accessibility for direct observation of the interior structure of crystal nuclei. A direct observation of the structure of growing 2D nuclei was made by Zhang *et al.*[17] Their observations were carried out in the AEF-controlled 2D colloidal system (Fig. 4a). They found that depending on supersaturation, the formation of nuclei may adopt different pathways in terms of structure evolution. To quantify the structure
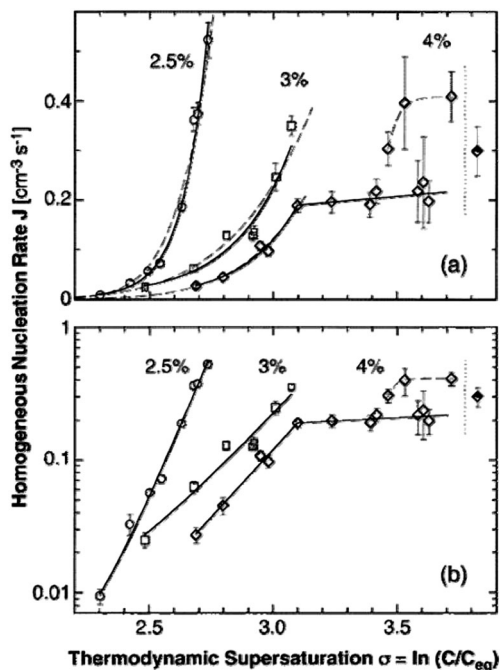
Fig. 8 Dependence of the rate J of homogeneous nucleation of lysozyme crystals on supersaturation σ at T = 12.6 °C and at three concentrations of the precipitant NaCl. Solid lines: fits with exponential functions; dashed lines: fits with the classical nucleation theory expression. Vertical dotted lines at σ = 3.9 (corresponding to lysozyme concentration 67 mg ml^{-1}) indicate the liquid–liquid coexistence boundary at this T and C_{NaCl} = 4%. (a) Linear coordinates; (b) semi-logarithmic coordinates. In agreement with the general expectations, the nucleation rate increases exponentially with supersaturation at each of the three precipitant concentrations. However, the dependence shows three peculiarities. (i) The $J(C)$ dependence at the highest precipitant concentration, C_{NaCl} = 4%, breaks at C^* = 33.5 mg ml^{-1}, and, in marked contrast to the prediction of eqn (17), the section above this concentration is practically steady as supersaturation increases. (ii) At $\sigma >$ 3.45 in the same $J(\sigma)$ dependence, the data scatter increases and three of the recorded points deviate significantly from the dominant trend. (iii) The nucleation rates are on the order of 0.1–1 cm^3 s^{-1}, which are about ten orders of magnitude less than the prediction of the classical nucleation theory. Reprinted with permission from ref. 77. Copyright (2000) American Chemical Society.
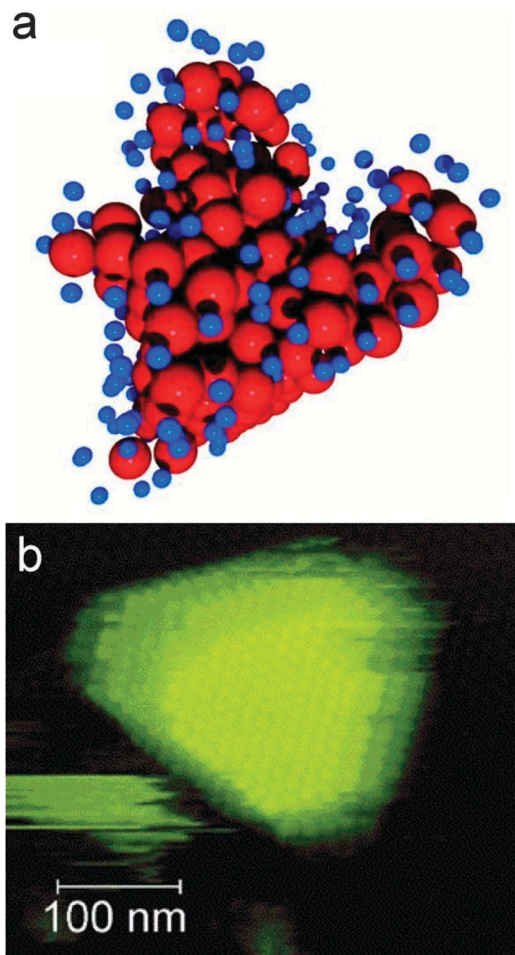

Fig. 9 Nonspherical crystal nuclei. (a) A snapshot of a crystallite of postcritical size in a poly(methyl methacrylate) sphere system. Red spheres represent crystal-like particles and are drawn to scale; the extra blue particles share at least one crystal-like ''bond'' with a red particle but are not identified as crystal-like and are reduced in size for clarity. (b) A nonspherical protein crystallite under AFM, which evolves from planar critical clusters. (a) From ref. 16. Reprinted with permission from AAAS. (b) Reprinted with permission from ref. 86. Copyright (2001) American Chemical Society.

of 2D nuclei, a local two-dimensional bond-order parameter is defined by

$$\psi_6(r_i) = M^{-1} \sum_j e^{i6\theta_{ij}} \quad (19)$$

where r_i is the mass center of particle i and θ_{ij} is the angle subtended between the vector connecting the particle i to its jth nearest neighbor and the arbitrary axis. M is the number of nearest neighbors of the particle i. The order degree of a particle is measured by $|\psi_6(r_i)|$. The mean value $\langle|\psi_6(r_i)|\rangle \sim 0.8$ in experimental 2D crystals is used as the criterion for crystal-like particles. In the studies, the interaction between colloidal particles was adjusted by adding salt (Na$_2$SO$_4$) with a concentration of 2×10^{-4} M.

At relatively low supersaturations (high frequencies), nuclei were created with a liquid-like structure (Fig. 10a, top left) and the fraction of crystal-like particles inside increases gradually as

they grow (Fig. 10a, top middle and right). The transition from the initial liquid-like structure to the final stable crystalline structure is a continuous process in terms of $\langle|\psi_6(r_i)|\rangle$ (Fig. 10a, bottom) which increases gradually with the size of nuclei and reaches a plateau of 0.8 (the average value for crystal-like particles) at a critical size. In contrast, at high supersaturations, nuclei adopt a crystalline structure from the beginning (Fig. 10b): $\langle|\psi_6|\rangle$ is as high as ~ 0.8 from the very beginning and remains stable during the growth. At intermediate super-saturations, for example ν = 3000 Hz and V_{pp} = 2.5 V (Fig. 3 in ref. 17), the structure of nuclei is flexible during the growth: the nuclei exhibit a crystalline structure at one time but become disordered subsequently. Only after the nuclei cross over a critical size, they become stable with the crystalline structure.

It follows from the above observations that the initial structure of crystal nuclei and the route to the final stable

This journal is © The Royal Society of Chemistry 2014

Chem. Soc. Rev., 2014, 43, 2324–2347 | 2335
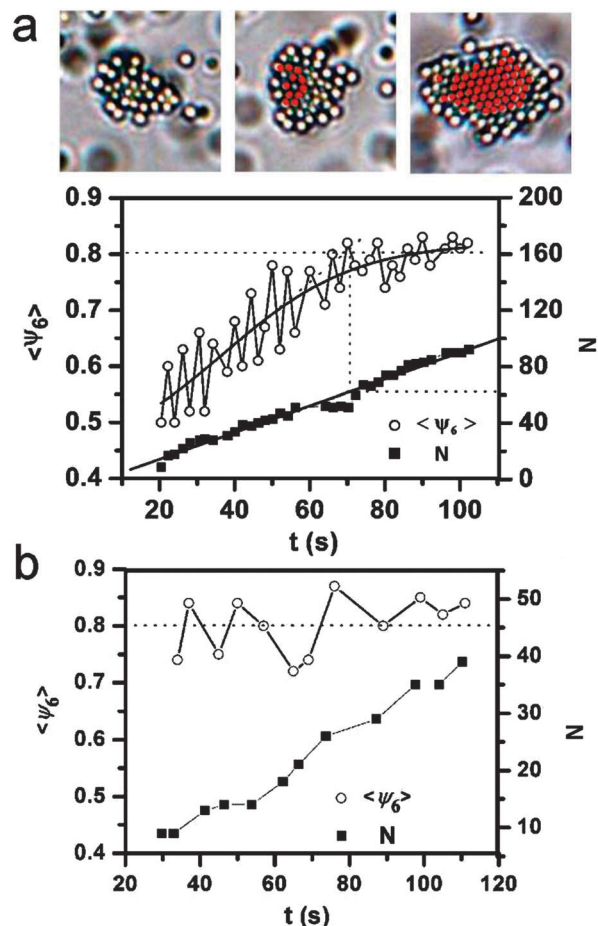
Fig. 10 Nucleation clusters. (a) Top: snapshots of a growing nucleus at a relatively low supersaturation: V_{pp} = 2.5 V, v = 5000 Hz. In the schematic representations, red particles represent crystal-like particles with $|\psi_6(r_i)|$ > 0.8 and blue particles represent liquid-like particles. The average bond-order parameter $\langle|\psi_6(r_i)|\rangle$ of nuclei increases gradually as a function of the size of nuclei and reaches a plateau at a critical size. (b) $\langle|\psi_6|\rangle$ as a function of the size of nuclei N at high supersaturations: V_{pp} = 2.5 V, v = 1000 Hz. Nuclei are created with a crystalline structure from the beginning. Adapted with permission from ref. 17. Copyright (2009) WILEY-VCH Verlag GmbH & Co. KGaA, Weinheim.

crystalline structures are supersaturation-dependent. At low supersaturations, metastable liquid-like structures are likely to occur first because they are easier to create due to the lower nucleation barrier for them.[17,90–92] At high supersaturations, the overall nucleation barrier for crystals is low. Correspondingly, the free energy difference between a metastable structure, for example a liquid-like structure, and the thermodynamically stable crystalline structure is small. If the difference is comparable to (or even smaller than) $k_B T$, it can be crossed over by thermal fluctuation. In this case, the effect of metastable structures in lowering the nucleation barrier becomes subtle; nuclei can adopt the stable structure from the beginning.

Multi-step crystallization

The formation of crystal nuclei from liquid is characterized by two transitions: the density transition from dilute to concentrated and
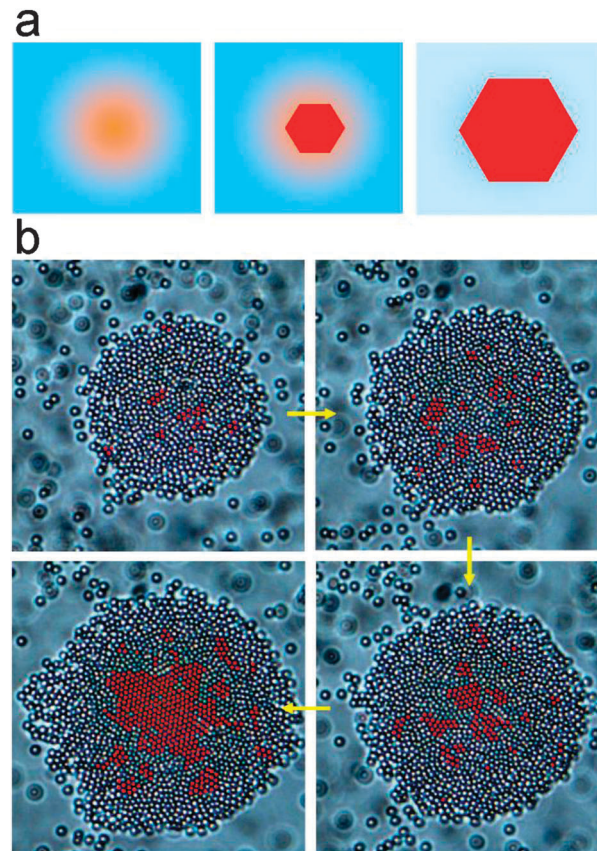
Fig. 11 Step-wise nucleation. (a) Two-step nucleation, which was suggested to occur in protein systems. Blue: dilute liquid phase. Yellow: dense liquid phase. Red: crystal phase. (b) Multi-step crystallization observed in the 2D colloidal system. The crystal-like particles defined by $\langle|\psi_6|\rangle$ > 0.8 are highlighted by red. Adapted with permission from ref. 18. Copyright (2007) American Chemical Society.

the structure transition from disordered to ordered. CNT assumes that the two transitions occur simultaneously. However, the simulations of ten Wolde and Frenkel revealed that in systems with short-range attractions, like proteins, nucleation of crystals may be a two-step process (Fig. 11a):[12] dense amorphous droplets are formed first through a liquid–liquid phase separation; crystalline nuclei are subsequently nucleated from the amorphous droplets. In the two-step nucleation, the structure transition and the density transition occur subsequently. The occurrence of the metastable amorphous phase can greatly reduce the nucleation barrier and enhance the nucleation of crystals. Experimentally, metastable amorphous phases have been observed broadly in biomineralization.[93,94] Biomineralization is the process by which organisms form a variety of functional crystalline structures. An intriguing feature of these functional crystalline materials is their well defined size and shape.[95,96] It is believed that the amorphous metastable phases in biomineralization not only reduce the nucleation barrier but also play a key role in precisely controlling the shape and the size of crystalline structures.[97] Recently it was suggested that two-step crystallization (TSC) may be a mechanism underlying most crystallization processes in typical

2336 | *Chem. Soc. Rev.*, 2014, **43**, 2324–2347

This journal is © The Royal Society of Chemistry 2014

atomic systems.[91,98] However, the kinetics of TSC remains unclear in these studies due to the absence of direct observations. To the best of our knowledge, the first experimental observation of TSC at the single-particle level was made in the AEF-controlled 2D colloidal system.

Fig. 11b presents a typical example of a multi-step crystallization (MSC) process observed in the 2D colloidal system.[18] Firstly, 2D dense amorphous droplets are created from the supersaturated solution (Fig. 11b, top left). As the amorphous droplets grow up, a few sub-crystal nuclei are created by fluctuation from the droplets (Fig. 11b, top right). However, the sub-nuclei are not stable and usually dissolve soon. New sub-nuclei are then created somewhere randomly (Fig. 11b, bottom right). The crystalline nuclei in the droplets have to reach a critical size N_{cry}^* before they can grow stably in the droplets. In experiments, every droplet can produce only one stable crystal (Fig. 11b, bottom left). Moreover, to form a stable crystal beyond N_{cry}^*, the droplets have to reach a critical size N^*. Although at the early stage many small dense droplets are created, only a few of them can reach the critical size N^* and successfully develop into a stable crystal. In MSC, the overall nucleation rate J_c of crystals can be determined by measuring the local rate j_c in the dense droplets.[99] The observation of MSC is consistent with previous observations in protein systems.[100]

CNT and Ostwald's rule

It is becoming increasingly clear that the properties, such as the shape and the structure, of nuclei in many cases are dependent on the size of nuclei and there are different routes for nuclei to reach final stable states. This picture is in contradiction to CNT. However, the presence of metastable crystalline structures or metastable amorphous phases is consistent with the so-called Ostwald's rule which dates back to one century ago. Ostwald's rule argues that the first nucleated phase is not necessarily the thermodynamically most stable one, but the one closest to the metastable liquid phase in terms of free energy[101,102] or the one having the lowest free energy barrier.[103] The liquid-like structures of sub-critical nuclei and the amorphous droplet in MSC have a smaller surface tension and thus a lower energy barrier. Kinetically, these metastable phases would be nucleated faster. Due to the occurrence of metastable intermediate structures or phases, the driving force and the energy barrier for nucleation are not constant during the formation of nuclei. As a consequence, CNT cannot be applied anymore to quantify MSC processes. The observations of supersaturation-dependent nuclei structure and MSC present experimental demonstrations of Ostwald's step rule. However, although Ostwald's step rule offers a general guideline for understanding the nonclassical nucleation routes, it is still a big challenge to establish a theoretical model which can quantitatively describe the effect of metastable structures and phases on nucleation.

The latest advance in the theoretical treatment of non-classical nucleation was reported by Baumgartner et al.[104] In their studies, the formation of magnetite in electrolyte solutions was visualized by cryogenic transmission electron microscopy (cryo-TEM). The observation found that mono-disperse primary particles were first formed from the super-saturated solutions, which subsequently fused into a crystalline phase. To take into account the impact of the primary particles on nucleation within the framework of CNT, Baumgartner et al. introduced an excess free energy term ΔG_p to bridge the gap between CNT and the non-classical pathway. The free energy change for nucleation from the primary particles is given by $\Delta \tilde{G}(R) = \Delta G(R) + \Delta G_p$. The sign of the excess free energy is positive if the primary particles are metastable and negative if they are stable. Whether nucleation occurs through a classical or non-classical pathway is determined by the relative bulk and surface energies of the amorphous and crystalline bulk phases together with the energetics of the primary particles. For example, if the energy barrier for the formation of crystalline phases is higher than that of amorphous phases ($\Delta G_C > \Delta G_A$), nucleation occurs via scenario (I) (Fig. 12a). Starting from the single particles, scenario (IV) will occur if the nucleation of a crystalline phase has a lower energy barrier than the nucleation of an amorphous phase ($\Delta \tilde{G}_A < \Delta \tilde{G}_C$). In this case, the nucleation of crystalline particles from the primary particles follows the same principle (classic nucleation theory) as the nucleation of primary particles from atoms or molecules. As a demonstration, this study shows that theoretically it is possible to fill the gap between the classical and non-classical nucleation routes within the classical framework, opening a door for future studies concerning the non-classical nucleation mechanism.

6. Crystal growth kinetics

Crystal growth takes place in the interfacial region between a crystalline phase and a fluid phase. The interfacial kinetics plays an essential role in controlling crystal growth and related phenomena, such as surface roughening, growth morphology, polymorphism, etc.[37,66,105–112] Fig. 13 presents a schematic illustration of a growing crystal surface which consists of flat regions, the so-called terrace, and steps. Two-dimensional nucleation on an existing terrace creates islands which produce new terraces and steps. (The dislocation in crystals offers another source of steps.[113]) The steps are usually zigzag due to the presence of kinks. Kink sites are the most stable positions for incoming atoms or molecules to attach because more bonds can be formed there. Kink sites can be created by thermally activated detachment or adatom absorption. As the number of molecules attaching to the crystal surface on average is larger than that detaching from the surface in a unit time, crystal growth occurs. The growth of crystals is represented by step advancing and the formation of new terraces. During the growth, the surface morphology, which is characterized by qualities such as the density of islands and the width of terraces, will greatly affect the quality of the resulting crystals. Dynamic processes, such as surface diffusion, step diffusion and mass transfer between terraces, play a critical role in determining surface morphology. These dynamic processes, to a large extent, are controlled by a set of energy barriers

This journal is © The Royal Society of Chemistry 2014

Chem. Soc. Rev., 2014, 43, 2324–2347 | 2337
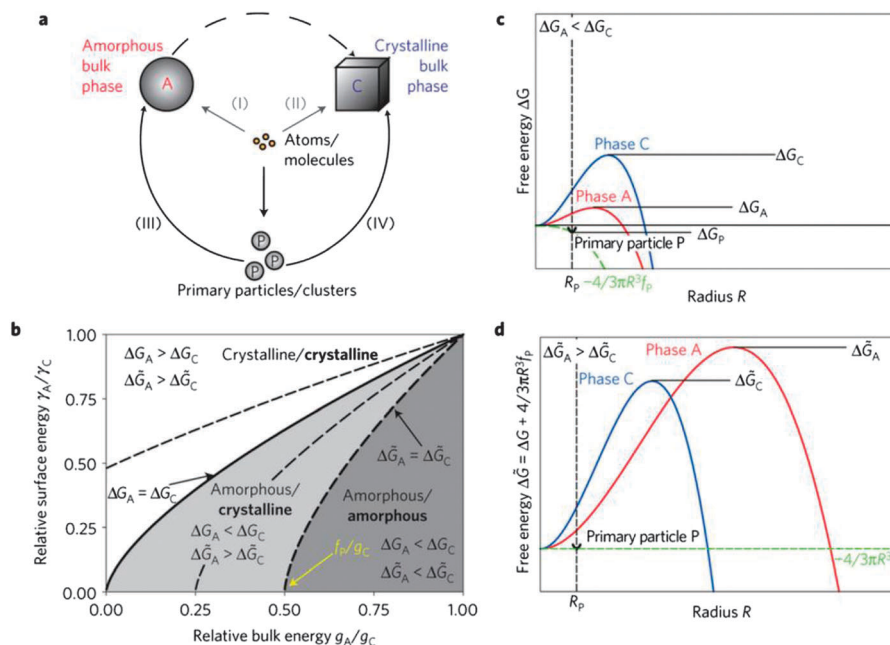
Fig. 12 Model crystallization scenarios from atoms/molecules and primary particles/clusters. (a) Scheme depicting the different pathways. (b) Phase diagram showing the parameter space for surface and bulk energy ratios that favor either amorphous- or crystalline-phase formation. The solid line indicates the boundary between phases for atom/molecule accretion scenarios; dashed lines indicate boundaries for primary particle/cluster accretion scenarios based on their stability f_P ($f_P/g_C = -0.25$, $f_P/g_C = 0.25$ and $f_P/g_C = 0.5$). g is the free energy gain per unit volume on formation of a nucleus and f is the energy density averaged over both surface and bulk energies. The favored phase by primary-particle accretion for an $f_P/g_C = 0.5$ scenario is given in bold letters, and by atomic accretion in regular letters. (c and d) Example ($\gamma_A/\gamma_C = 0.4$; $g_A/g_C = 0.5$; $f_P/g_C = 0.35$) in which primary-particle stability reverses the energy-barrier heights from a step-rule scenario (c; amorphous before crystalline) to direct crystal formation (d) when forming by primary-particle accretion instead of atomic/molecular accretion. The green dashed lines (curve in c) indicate the energy content of the consumed primary-particle aggregate ($-4/3R^3 f_P$), augmented to the free energy of the bulk phases in (d). Reprinted with permission from Macmillan Publishers Ltd: Nat. Mater. (ref. 104), copyright (2013).
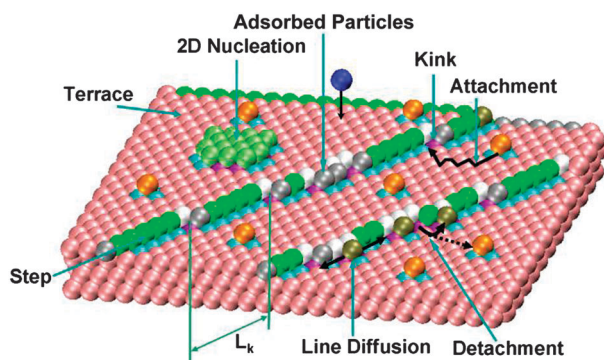

Fig. 13 Atomic processes on the surface of a growing crystal.

which are determined by the strength of bonds between molecules, in other words, the interaction between molecules.

Understanding the effect of various dynamic processes on surface morphology is critical for applying effective control on the growth to achieve desired products. However, direct observation of the dynamic processes is difficult in atomic systems. Recently, it was illustrated that the dynamic processes in colloidal crystal growth follow the same principles as those obeyed by atoms.[114] In crystallizing colloidal model systems, direct observations at the single-particle level are experimentally accessible.

Step kinetics

In practice, a smooth surface is extensively required in developing advanced thin film materials. For example, in epitaxial growth, smooth growth or 2D growth is observed at high temperatures when the interlayer transport is active. At low temperatures when the interlayer transport is inhibited by a step-edge energy barrier, the so-called Ehrlich–Schwoebel (ES) barrier, rough surfaces will be formed.[115,116] On the theoretical ground, it is important to establish a correlation between surface morphology and surface dynamic processes. However, visualization of the dynamic processes at the atomic level is experimentally inaccessible yet. So far, the related studies were mainly conducted by simulations. While colloidal model systems have been widely employed in studying nucleation, they were recently used to study epitaxial growth by Ganapathy *et al.*[114] In their studies, the nucleation and growth of colloidal crystal films were investigated. The observation shows that the growth of 2D colloidal crystal films exhibits island nucleation and growth (Fig. 14C and D) which obey similar laws as that in atomic systems: the distribution of residence time shows that there is a step-edge energy barrier which confines the diffusion of free monomers (Fig. 14G and H); the relation between the saturation island density and the surface diffusion constant is well described by the same power law associated with the step-edge barrier.
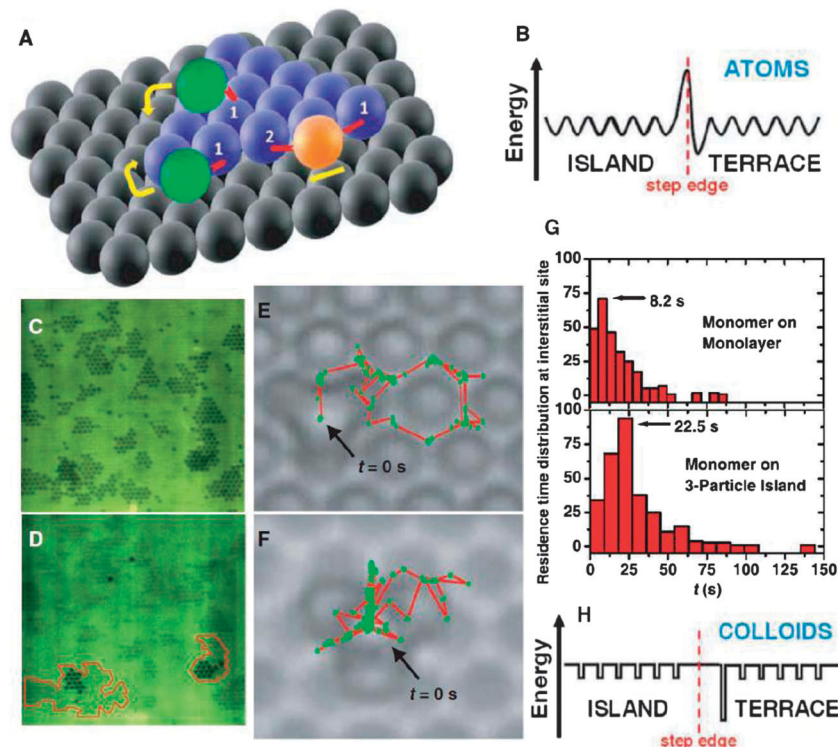
Fig. 14 Step kinetics in colloidal crystal growth. (A) Schematic of an adatom diffusing near an island step edge. (B) Energy landscape for atoms near a step edge. (C) Image of islands growing on the monolayer substrate. (D) Image of islands nucleating on top of islands shown in (C) (red outline). The separation between islands in (C) is ≈8.0 lattice constants, whereas the radius of the islands in (D) is ≈2.5 lattice constants. (E) Polystyrene colloid diffusing on a colloidal monolayer with a triangular symmetry. The trajectory of the colloid during a 180 s interval is shown in red with green dots. (F) Trajectory of a polystyrene colloid diffusing on a three-particle island over 180 s. Island rearrangements in experiments are rare. (G) Interstitial residence time distribution for a colloidal particle diffusing on a monolayer (top) and for a particle diffusing on a three particle island (bottom). (H) Energy landscape for colloids near a step edge. From ref. 114. Reprinted with permission from AAAS.
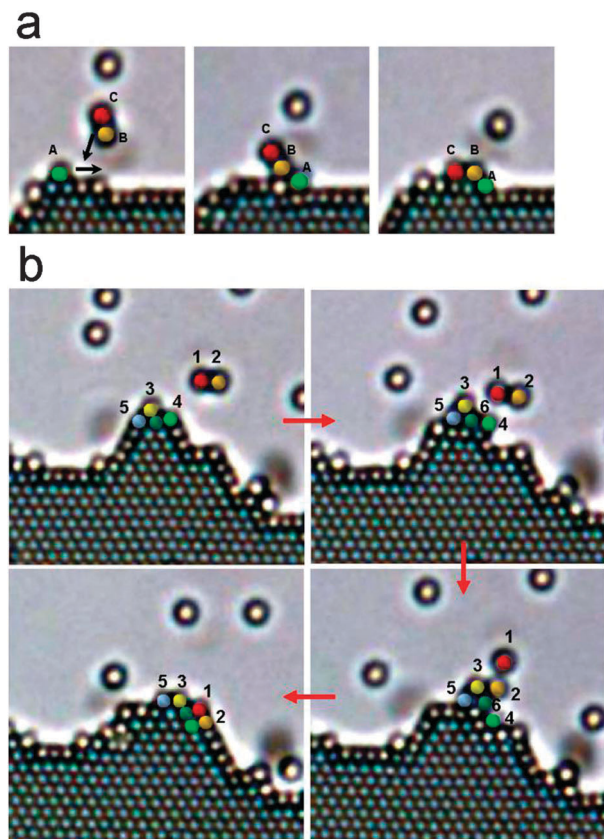
An intriguing phenomenon in epitaxial growth is the so-called reentrant smooth growth: normally smooth growth occurs generally at high temperatures. However, it was found recently that the smooth growth occurs unexpectedly as temperature is lower than a certain value.[117] This is similar to the phenomina observed in the growth of *n*-paraffin crystals from solutions.[105,106] To address the reentrant smooth growth, downward funneling (DF) was suggested.[118] The DF mechanism argues that atoms deposited beyond a step edge would like to funnel down to lower layers with their condensation energy. On the other hand, van Dijken *et al.* found by simulations that because of the attraction between growing fronts and incoming atoms,[119] incoming atoms are preferentially adsorbed on the top of existing islands, which is known as the steering effect. The steering effect tends to undermine the effect of DF.[120] However, the DF mechanism has been widely used to explain the reentrant smooth growth.[118,121,122] If the DF mechanism is suppressed by the step-ad-atom attraction, the re-entrant smooth growth has to be understood with a different mechanism.

To address the mechanism of the reentrant smooth growth in the presence of the steering effect, the dynamic processes of incorporation were investigated in the AEF-controlled 2D colloidal system. It was found that the steering effect suggested

by simulations[119,120] reflects only one side of the feature of step-adatom attractions. In these studies, incoming atoms were assumed to arrive at steps one by one and the rearrangement of step atoms was inhibited during the incorporation. However, this presumption does not hold true in real experiments. Fig. 15 presents two typical descending processes in 2D colloidal crystal growth.[47] Fig. 15a presents the early stage of an adatom incorporation process: the dimer consisting of particles *B* and *C* is approaching a step on which a mobile monomer *A* stays. As the monomer feels the attraction from the dimer, it is accelerated towards the right (Fig. 15a, middle). Facilitated by the acceleration, the monomer *A* crosses over the step edge and descends to the 'lower' layer (Fig. 15a, right). It follows that it is possible for the attraction between incoming particles and absorbed particles to induce an additional descending transport, being opposite to the effect of the steering effect.

Fig. 15b presents a more complex step incorporation process. The particles numbered from 3 to 6 form the top of a step peak; the dimer consisting of particles 1 and 2 is approaching (Fig. 15b, top left). As the trajectory of the dimer is directed toward the step peak by the attraction from the step particles, step particles 3–6 are accelerated (Fig. 15b, top right). From the acceleration, particles 4 and 6 acquire excess dynamic energy to cross over the step edge and descend to the 'lower' layers

This journal is © The Royal Society of Chemistry 2014

Chem. Soc. Rev., 2014, **43**, 2324–2347 | **2339**

Fig. 15 (a) Descending transport triggered by the attraction from the incoming dimer. (b) Smoothing effect of the attraction from the incoming dimer. Step particles are pulled down by the incoming dimer, resulting in reduction of the local roughness. Adapted with permission from ref. 47. Copyright (2007) American Chemical Society.

(Fig. 15b, bottom right). After the process, the incoming dimer is incorporated into the upper step and the step becomes smoother.[47]

The above observations demonstrate that the importance of attraction between the incoming particles and the growing front is twofold: it can induce a steering effect and, simultaneously, it can also activate a smoothing process. The steering effect enhances the growth of step protrusion while the smoothing process transports particles on the upper layer down to the lower layers. At high temperatures, the DF mechanism dominates. At low temperatures, the surface becomes rough and the islands are smaller. The particles on the top of islands are closer to step edges and, therefore, can more readily descend down to the lower layers once they are accelerated by incoming clusters. In practice, cluster absorption or deposition may enhance the smoothening effect.

Cluster adsorption

In the classical treatment of crystal growth, the growth units are generally simplified as monomers. However, as illustrated in Fig. 15, the growth may occur through cluster adsorption. To address the general principle of cluster adsorption, the growth of a 2D colloidal crystal near line templates was monitored.[123] At the very initial stage, the colloidal particles were randomly dispersed in the solution (Fig. 16b: 0 s); upon the application of AEF of a frequency of 800 Hz and a field strength $E_{pp} = 4.0 \times 10^4$ V m^{-1}, a stable crystal is formed immediately on the line templates, while in the regions far away from the line templates, a number of colloidal clusters are formed in a short time (Fig. 16b, $t = 2.6$ s). The clusters keep moving till they incorporate
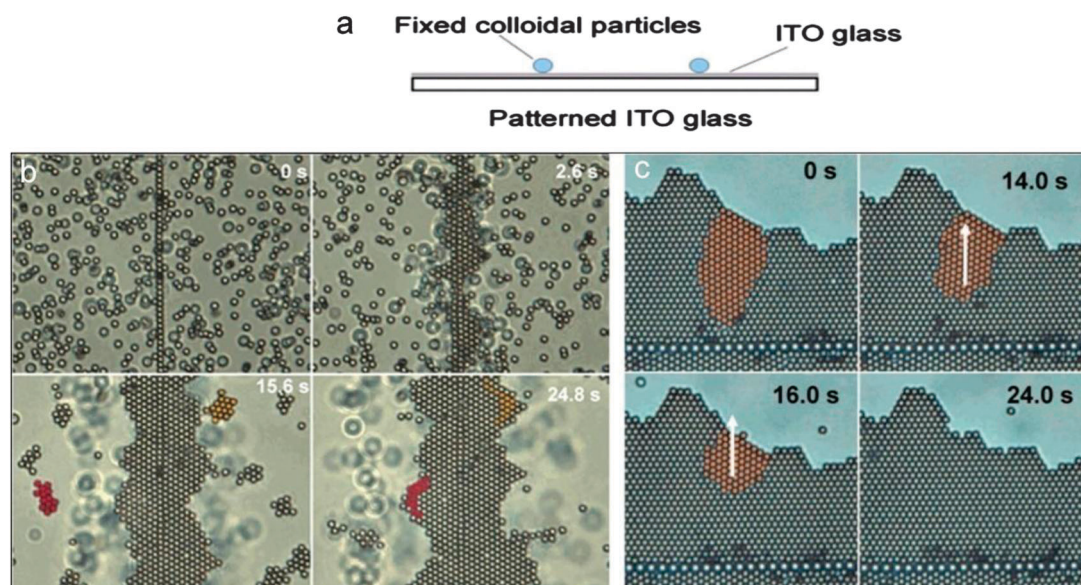
Fig. 16 (a) Schematic illustration of the line templates for 2D colloidal crystals. (b) Snapshots of the epitaxial crystallization of 1.8 μm colloidal particles near line templates which are fabricated with identical colloidal particles. Frequency v = 800 Hz; field strength $E_{pp} = 4.0 \times 10^4$ V m^{-1}. Two clusters undergoing incorporation are highlighted by yellow and red respectively. (c) The evolution of a misoriented grain in a colloidal crystal composed of 1.8 μm colloidal particles and a 3.0 μm artificial linear defect, during a controllable annealing process by decreasing the frequency from 1000 to 600 Hz. (a) Reprinted with permission from ref. 44. Copyright (2012), WILEY-VCH Verlag GmbH & Co. KGaA, Weinheim. (b and c) Adapted with permission from ref. 123. Copyright (2009) American Chemical Society.

into the growing crystal. After the initial fast growth, the following growth mainly proceeds *via* cluster absorption (Fig. 16b: 15.6 s). During the incorporation, the structure and the shape of clusters are flexible. In the resulted crystals, defects were rarely observed. The local melting induced by the impact of incoming clusters may play a key role in annealing the growing front.

In another study, the line templates were fabricated with particles of diameter 3.0 μm while the colloidal particles dispersed in the solution for crystallization had a diameter of 1.8 μm. During the crystallization, due to the mismatch of the lattice constant, as shown in Fig. 16c, grain boundaries were formed. However, upon decreasing the frequency from 1000 to 600 Hz, the grain boundary was removed. This process can be regarded as self-perfection. Self-perfection can be understood in that decreasing frequency increases the strength of attraction between neighbouring particles which become bonded more closely. Accompanying the decrease in the lattice constant, a global rearrangement is activated, which enhances the diffusion of grain boundaries.

Surface roughening

At low temperatures, the energy associated with the creation of a step on a crystal surface is non-zero.[111] The formation of a new layer on an existing layer at crystal surfaces has to overcome a free energy barrier, the so-called 2D nucleation barrier. Therefore, creation of new islands is not preferred, giving rise to an overall flat surface.[124,125] Dislocations offer another natural step resource for crystal growth at low temperatures.[124,125] However, if the crystals are free of dislocations, the growth is then governed completely by 2D nucleation[66,111,126] and the growth rate is determined by the 2D nucleation rate. Above a temperature, the so-called roughening transition temperature T_R, the free energy needed to create a step becomes negligible and new steps or kinks can be created even in the absence of screw dislocations. In this case, the growing surface becomes rough.

The roughening transition has been studied extensively by computer simulations[111,125,126] based on the so-called solid-on-solid (SOS) interfacial model which is a generalization of the Ising model. The SOS model assumes that the crystal surface is a collection of interacting columns. The corresponding Hamiltonian can be expressed as

$$H = \gamma_E \sum_{\langle ij \rangle} |h_i - h_j|^2 \qquad (20)$$

Here γ_E is the step energy per unit length and h_i is the column height. According to this model, the roughening transition is a typical Kosterlitz–Thouless (KT) type[105,127] in terms of the step free energy γ which decreases continuously as the temperature approaches the roughening transition temperature:

$$\gamma \sim \exp[-\alpha(T_R - T)^{-1/2}] \text{ as } T \to T_R \ (T < T_R) \qquad (21)$$

However, experimental observations show that the roughening transition can be of infinite order or first order.[66,105,111,124–127] Although computer simulations have acquired images at the single-particle level, experimental observations were absent for a
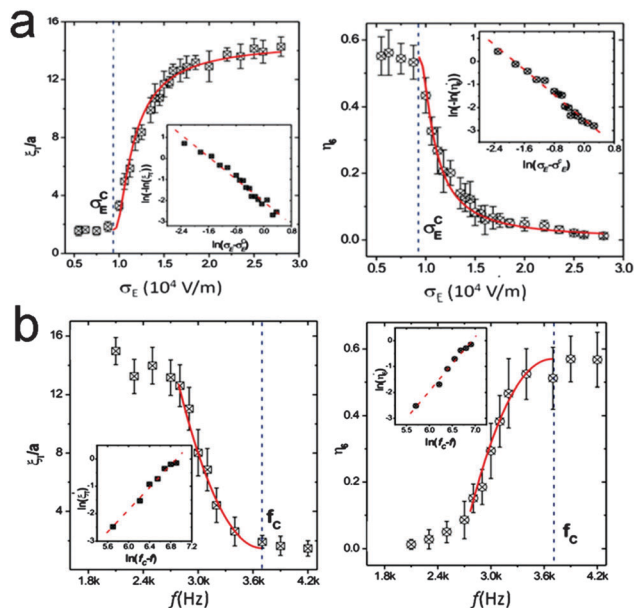

Fig. 17 (a) The translational correlation length ξ_T (left) and the bond-orientational order η_6 (right) measured at different external field strength ranging from 2.8×10^4 V m^{-1} to 0.5×10^4 V m^{-1} at the frequency $f = 0.8$ kHz. Here the position of the vertical dotted line is the critical strength $\sigma_E^C = 0.9 \pm 0.05 \ 10^4$ V m^{-1}. The ln–ln plots of the normalized order parameters ξ_T' and η_6' against $\ln(\sigma_E - \sigma_E^C)$ are shown in the insets in the right corner. The straight dotted line in each inset is the least-squares fit of the data. Fitting parameters (left): $\ln(\alpha) = -2.055 \pm 0.058$, $\beta = -1.33 \pm 0.061$. Fitting parameters (right): $\ln(\alpha) = -2.518 \pm 0.057$, $\beta = -1.350 \pm 0.058$. The red curves are the best fits of the exponential function with the given fitting parameters. (b) The parameters ξ_T and η_6 measured at different frequencies ranging from 2.1 kHz to 4.2 kHz at a fixed field strength $\sigma_E = 2.8 \times 10^4$ V m^{-1}. The position of the vertical dotted line is the critical frequency $f_c = 3.7 \pm 0.1$ kHz. The ln plots of the normalized order parameters ξ_T' and η_6' against $\ln(f_c - f)$ are shown in the insets in the left corner. The straight dotted lines in the insets are the least-squares fits of the data. Fitting parameters: $\lambda = 2.04 \pm 0.07$ (left) and $\lambda = 2.09 \pm 0.11$ (right). The red curves are the best fits of the power-law function with the given fitting parameters. Adapted with permission from ref. 24. Copyright (2006) by The American Physical Society.

long time. In this regard, the AEF-controlled 2D colloidal system offers an ideal model for studying the roughening transition at the crystal surface.

A 2D colloidal crystal can be regarded as a growing crystal layer on an existing crystal surface. In this system, the phase transition from an isotropic suspension to a highly ordered colloidal monolayer can be initiated and controlled.[24] In the context of modelling, this is a typical case of the 2D Ising model. Distinct from the SOS model, the order–disorder transition of the 2D Ising model should be a second order phase transition.[127] To our surprise, the observations on such a 2D colloidal crystal layer show that the strength-dependent phase transition is an infinite-order transition (Fig. 17a) while the frequency-dependent phase transition is a second-order one (Fig. 17b).[24] To the best of our knowledge, both the infinite-order and the second-order surface roughening transition at the two layer solid–fluid interface have never been recognized before this study.

7. Crystal branching and network formation

Crystal branching occurs in a variety of systems and plays a critical role in developing fibre network materials which have extensive applications in photography, cosmetics,[128] drug delivery[129,130] and fabrication of nanostructures.[131,132] Crystal branching is usually associated with high supersaturations and the presence of internal crystal defects. In branching, sub-crystals are developed on existing crystals but with deviated orientations. Therefore, crystal branching is ubiquitously associated with structural mismatch and heterogeneous nucleation. In heterogeneous nucleation, as discussed in Section 4.1, substrates can effectively lower the nucleation barrier and promote the formation of nuclei. The efficiency of the substrates depends on parameters such as crystal structure, lattice mismatch and supersaturation. At high supersaturations as the nucleation barrier becomes low, the effect of substrates in lowering the nucleation barrier becomes insignificant and branching with structural mismatch often occurs.

Interfacial structure mismatch nucleation

In addition to lower nucleation barrier, the occurrence of substrates also exerts a negative impact on the surface integration, the so-called shadow effect: substrates can reduce the effective collisions of structural units with the surface of clusters. As a result, nucleation kinetics becomes slower and the effect of substrates in lowering the nucleation barrier is partly weakened. These two competing effects of substrates have different consequences in different regimes. At low supersaturations, the nucleation barrier is high and thus the role of substrates in reducing the nucleation barrier is significant. In this case, the interaction between the substrates and the nucleating phase becomes critical. A structural synergy between the nucleating phase and the substrate gives rise to the most reduction of nucleation barrier. Therefore, heterogeneous nucleation is kinetically favoured.[108,109]

At high supersaturations, the nucleation barrier is small. The role of substrates in lowering the nucleation barrier becomes subtle. Instead, the shadow effect becomes dominant. For nuclei having larger $f(m)$ and $f'(m)$ (or $m \to 0$, -1), the orientation freedom is high. A high orientation freedom could substantially reduce the shadow effect and promote the growth of nuclei. In this case, the interfacial structural mismatch between nuclei and substrates is kinetically favoured due to the resulted faster nucleation kinetics. Interfacial structural mismatch nucleation has been found to play a very important role in the pattern formation, crystallite network formation, and supermolecular soft materials formation.[63,133–135] However, despite its broad interests, direct experimental verification of the templating and the supersaturation-driven interfacial structural mismatch is rare.

Recently, using the AEF-controlled 2D colloidal system, Xie and Liu successfully made a direct observation of the effect of templates on structural mismatch.[110] In their study,
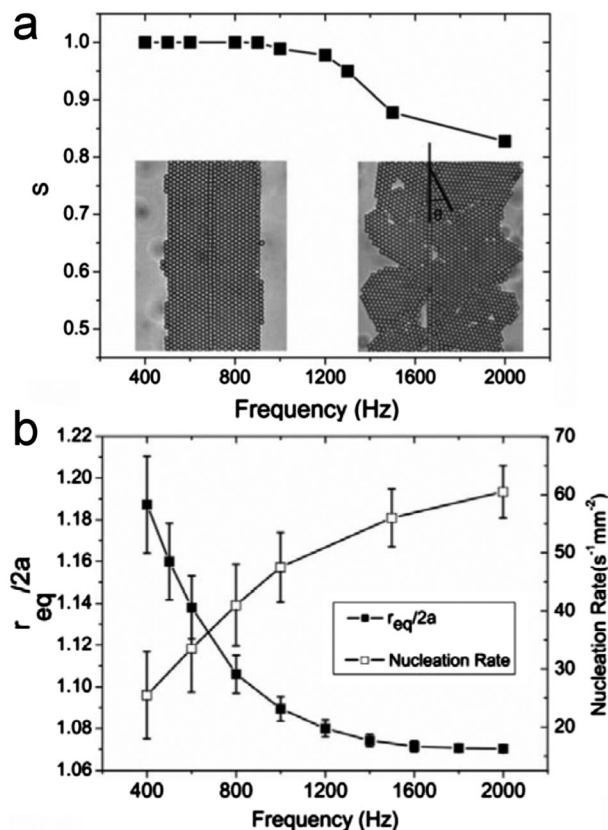

Fig. 18 Heterogeneous 2D colloidal crystallization. (a) Frequency dependence of the orientational order parameter. Left inset: $S = 1$ at 800 Hz; right inset: $S = 0.83$ at 1000 Hz. (b) Variation of the equilibrium distance and nucleation rate in the bulk fluid phase as a function of frequency. The diameter of the colloidal particles is 1.8 μm. Adapted with permission from ref. 123. Copyright (2009) American Chemical Society.

line templates as illustrated in Fig. 16a are used to induce heterogeneous nucleation. Therein, an orientational order parameter $S = 1/2\langle 3\cos^2\theta - 1\rangle$ is used to quantify the uniaxial ordering of the colloidal assembly. Here, the misfit angle θ of a crystal domain is defined in reference to the line templates (the right inset in Fig. 18a). The brackets denote that the parameter S is an average of $3\cos^2\theta - 1$ over all of the particles in the assembly. One has $S = 1$ as the orientation of a crystalline domain is parallel to the line template. Fig. 18a presents the measured S as a function of frequency. There are two distinct regions. High quality crystals free of defects ($S = 1$) are obtained in the low frequency region of 400–800 Hz. At high frequencies (1000–2000 Hz), the quality of crystals in terms of S becomes worse upon increasing the frequency. Correspondingly, the measured interparticle separation r_{eq} in the crystalline domains decreases upon increasing the frequency. At the same time, the nucleation rate increases as the frequency increases. It follows that increasing frequency leads to a stronger attractive force between particles and thus smaller nucleation barriers.[123] Therefore, the reduced degree of perfection of the colloidal crystals and the mismatch with the template can be considered as a supersaturation-driven interfacial structural mismatch effect.

8. Defect formation and dynamics

In practice, a variety of defects are created inevitably during the growth of crystals. The defects play a key role in determining the performance of crystals. For example, the electrical and optical properties of crystals are strongly associated with dislocations; the presence of vacancies can enhance atom diffusion in crystals.[136] Understanding the diffusion of defects and the interaction between defects is of great importance in condensed-matter physics and material sciences.[137] In atomic systems, however, it is a challenge to directly track defects. As an alternative approach, colloidal crystals were employed as model systems for studying crystal defects.[138,139] For example, in a 2D colloidal crystal system with strong electrostatic interaction, point defects were created by optical tweezers (Fig. 19a).[139] Both monomer and dimer vacancies exhibit global diffusion in the 2D colloidal crystal. The dimer vacancies can dissociate into pairs of well-separated dislocations. The diffusion of dimer vacancies is enhanced by the dissociation and is faster than that of the monomer vacancies. More importantly, it was found that the hopping of the defects is not a pure random walk, but exhibits surprising memory effects. In another work concerning

point defects, configurations and diffusion of defects were studied in the AEF-controlled 2D colloidal system, where the interactions between colloidal particles in the crystal are attractive.[46] In this system, the monomer vacancies are immobile. For dimer vacancies as shown in Fig. 19b (left top), two stable configurations were identified as threefold symmetric (D_3) and twofold symmetric (D_2). The relative occurrence probabilities of D_2 and D_3 are found to be 0.47 ± 0.01 and 0.53 ± 0.01 respectively. Based on the relative probability, the free energy difference $\Delta\varepsilon$ between configurations D_2 and D_3 is measured as $\sim 0.12\ k_B T$. Similarly, trimer vacancies also exhibit two kinds of configurations as shown in Fig. 19b (left bottom) and have threefold symmetry D_3 and twofold symmetry D_2 as well. For trimer vacancies, the relative occurrence probability of D_3 is higher than that of D_2 as well. It follows that for vacancies, configurations with higher symmetry are more stable. The vacancies diffuse in the crystals by hopping from one configuration to another configuration. For dimer vacancies, the trajectories of particles around the vacancies are interconnected. It follows that during the configuration transformation, particles can hop from one lattice-site to a neighbor site and, therefore, dimer vacancies can diffuse globally in the crystals.
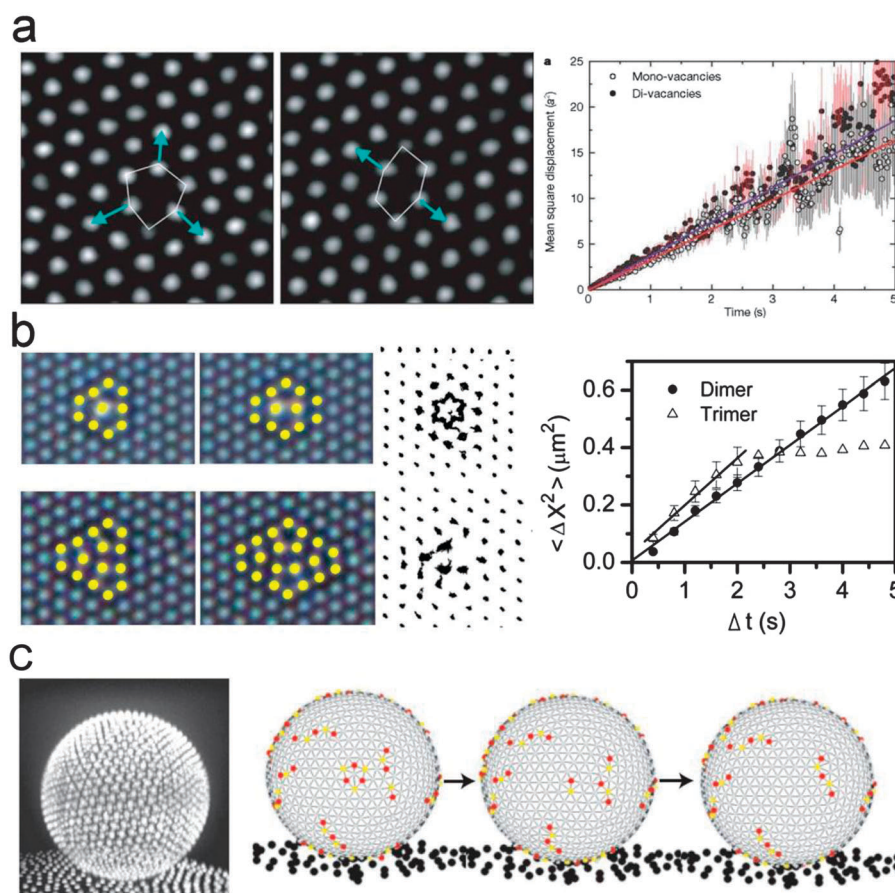
Fig. 19 Defects in 2D colloidal crystals. (a) Diffusion of vacancies in repulsive colloidal crystals. (b) Configuration and diffusion of defects in attractive colloidal crystals. (c) Behavior of interstitials on a curved surface. (a) Adapted with permission from Macmillan Publishers Ltd: Nature (ref. 139), copyright (2001). (b) Adapted with permission from ref. 46. Copyright (2006) AIP Publishing LLC. (c) Adapted with permission from Macmillan Publishers Ltd: Nat. Mater. (ref. 141), copyright (2009).

This journal is © The Royal Society of Chemistry 2014

Chem. Soc. Rev., 2014, 43, 2324–2347 | 2343

However, for trimer vacancies, the trajectories exhibit no hopping between lattice-sites and no global diffusion is observed as the mean square displacement reveals.

Combining the above observations, it follows that the behavior of point defects is strongly dependent on the feature of colloidal interactions. In repulsive colloids, both monomer vacancies and dimer vacancies are mobile; dimer vacancies can dissociate into a dislocation pair. In attractive colloids, monomer vacancies are immobile and the mobility of dimer and trimer vacancies is remarkably lower than that of repulsive colloids. Since in typical atomic systems, the interaction between neighboring atoms can be modelled by an attractive potential, the behavior of defects in atomic systems should be analogous to that in attractive colloids. This is supported by the observations in graphene layers in which monomer vacancies were found to be immobile under normal conditions[136] and in the simulation,[137] the diffusion of monomer vacancies is active only at extremely high temperatures (>3000 K).

Two-dimensional crystalline ordering on a curved surface is an interesting topic related to fields including the formation of vesicles and biological membranes.[140] To explore the properties of defects on a curved surface, a 2D colloidal crystal on a curved surface was developed recently by Irvine et al.[141,142] In their studies, 2D colloidal crystals were formed on a curved oil/oil interface. Using optical tweezers, interstitials were inserted into the 2D colloidal crystals. The interstitials are generally absorbed by grain boundaries (Fig. 19c): the absorption proceeds through local structure rearrangement if the interstitials are close to a grain boundary; if the interstitials are far away from grain boundaries, they usually dissociate into dislocation pairs which keep gliding till they are absorbed by grain boundaries.

As illustrated by the above examples, the modelling based on controlled colloidal assembly opens up a new pathway for studying the dynamics of defect formation. In this regard, there are still fundamental problems under exploration, such as the diffusion of grain boundaries during annealing processes and the interaction between point defects. The study based on colloidal model systems is expected to advance our understanding of these problems.

9. Conclusions and perspectives

In this review, we summarize the recent progress in understanding the fundamental aspects of crystallization, based on controlled colloidal assembly, in particular, employing an AEF-controlled colloidal system. This is an experimental modelling technique that combines the visualization and the quantitative treatment.

Almost all fundamental aspects of crystallization were examined in the experimental modelling systems. For instance, although it has been confirmed that the classical nucleation theory can be applied to describe the main feature of nucleation dynamics in a steady state, the initial stage of nucleation deviated from the theory in many cases. The fact that nature always selects dynamically the most-easy path has been

demonstrated unambiguously in nucleation. Unlike the assumption that both the embryos and the bulk crystals share the same structure, the structures of the embryos are supersaturation-dependent. Such a deviation would be beneficial in lowering the nucleation barrier, and then facilitate the nucleation kinetics at low supersaturations. Concerning the solid–fluid interface, the experimental modelling has also provided some extremely relevant information. For example, a cluster consisting of a few growth units can be incorporated into the steps without causing any defect. In this process, the self-orientation of the clusters plays an important role. In recent years, the concept of supersaturation-driven structural mismatch has been put forward in describing mesophase assembly. Nevertheless, it has never been confirmed directly before. The templated 2D colloidal nucleation provides the first observation of this effect at the single-particle level. As demonstrated, this experimental modelling technique has been successfully applied to examine many other crystallization processes, i.e., multi-step crystallization, roughening transition, adatomic step integration, defect generation and migration kinetics, etc., which have never been examined quantitatively before at the single-particle level. Previous theoretical analyses and computer simulations only predict that the infinite-order surface roughening transition can occur in the solid-on-solid multi-layer mode while one can only have a second-order phase transition at the two-layer solid–fluid interface. The experimental modelling, however, indicates that we can have both the infinite-order and the second order surface roughening transition at the two-layer solid–fluid interface if we choose different parameter sets. This allows us to check the theories directly.

Based on this experimental modelling technique, the following problems in the field of crystallization can be further addressed at the single-particle level.

Oriented attachment (OA). OA has been suggested as another important mechanism for nuclei/nanocrystal growth.[143,144] In the mechanism of OA, nanocrystals will first align spontaneously with common crystallographic facets and then coalesce irreversibly. Usually, the attachment is observed primarily at the higher-energy surfaces which can effectively decrease the overall free energy. Although OA has been studied extensively, some basic principles of OA are still open to questions.[145]

Heterogeneous nucleation. Although there are a number of discussions concerning the mechanism of heterogeneous nucleation, to the best of our knowledge, still many questions are to be addressed. By pinning colloidal clusters on the surfaces where crystallization occurs, one can examine systematically how the size and the shape of the clusters as the nucleation centers will affect the nucleation process.

Grain boundary dynamics. The key questions to be addressed include the following: how grain boundaries diffuse as a collection of dislocations; how grain boundaries determine their diffusion route; how they will interact when two grain boundaries meet; how they anneal; etc.

The problems listed here are of fundamental importance for controlling the growth of crystals. Moreover, a full understanding of their principles can also facilitate the fabrication of nanocrystals.

Acknowledgements

References

1 G. H. Gilmer and P. Bennema, *J. Cryst. Growth*, 1972, **13–14**, 148–153.

2 G. H. Gilmer and P. Bennema, *J. Appl. Phys.*, 1972, **43**, 1347–1360.

3 C. C. Battaile, *Comput. Methods Appl. Mech. Eng.*, 2008, **197**, 3386–3398.

4 T. P. Schulze, *J. Comput. Phys.*, 2008, **227**, 2455–2462.

5 M. Nicholas, W. R. Arianna, N. R. Marshall, H. T. Augusta and T. Edward, *J. Chem. Phys.*, 1953, **21**, 1087–1092.

6 J. Anwar and D. Zahn, *Angew. Chem., Int. Ed.*, 2011, **50**, 1996–2013.

7 B. J. Alder and T. E. Wainwright, *J. Chem. Phys.*, 1959, **31**, 459–466.

8 M. Matsumoto, S. Saito and I. Ohmine, *Nature*, 2002, **416**, 409–413.

9 M. P. Allen and D. J. Tildesley, *Computer Simulation of Liquids*, Oxford University Press, Oxford, 1989.

10 D. Frenkel and B. Smit, *Understanding Molecular Simulation*, Academic Press, London, 1996.

11 S. Auer and D. Frenkel, *Nature*, 2001, **413**, 711–713.

12 P. R. ten Wolde and D. Frenkel, *Science*, 1997, **277**, 1975–1978.

13 S. Auer and D. Frenkel, *Nature*, 2001, **409**, 1020–1023.

14 V. J. Anderson and H. N. W. Lekkerkerker, *Nature*, 2002, **416**, 811–815.

15 P. N. Pusey and W. van Megen, *Nature*, 1986, **320**, 340–342.

16 U. Gasser, E. R. Weeks, A. Schofield, P. N. Pusey and D. A. Weitz, *Science*, 2001, **292**, 258–262.

17 T. H. Zhang and X. Y. Liu, *Angew. Chem., Int. Ed.*, 2009, **48**, 1308.

18 T. H. Zhang and X. Y. Liu, *J. Am. Chem. Soc.*, 2007, **129**, 13520–13526.

19 U. Gasser, *J. Phys.: Condens. Matter*, 2009, **21**, 203101.

20 G. L. Hunter and E. R. Weeks, *Rep. Prog. Phys.*, 2012, **75**, 066501.

21 Z. Zhang, P. J. Yunker, P. Habdas and A. G. Yodh, *Phys. Rev. Lett.*, 2011, **107**, 208303.

22 K. N. Pham, A. M. Puertas, J. Bergenholtz, S. U. Egelhaaf, A. Moussaid, P. N. Pusey, A. B. Schofield, M. E. Cates, M. Fuchs and W. C. K. Poon, *Science*, 2002, **296**, 104–106.

23 Y. Peng, Z. Wang, A. M. Alsayed, A. G. Yodh and Y. Han, *Phys. Rev. Lett.*, 2010, **104**, 205703.

24 K.-Q. Zhang and X. Y. Liu, *Phys. Rev. Lett.*, 2006, **96**, 105701.

25 P. N. Pusey, E. Zaccarelli, C. Valeriani, E. Sanz, W. C. Poon and M. E. Cates, *Philos. Trans. R. Soc., A*, 2009, **367**, 4993–5011.

26 C. Rascon, E. Velasco, L. Mederos and G. Navascues, *J. Chem. Phys.*, 1997, **106**, 6689–6697.

27 A. U. Borwankar, A. K. Dinin, J. R. Laber, A. Twu, B. K. Wilson, J. A. Maynard, T. M. Truskett and K. P. Johnston, *Soft Matter*, 2013, **9**, 1766–1771.

28 E. Zaccarelli, *J. Phys.: Condens. Matter*, 2007, **19**, 323101.

29 T. H. Zhang, J. Klok, R. Hans Tromp, J. Groenewold and W. K. Kegel, *Soft Matter*, 2012, **8**, 667–672.

30 F. Li, D. P. Josephson and A. Stein, *Angew. Chem., Int. Ed.*, 2011, **50**, 360–388.

31 A. Yethiraj, *Soft Matter*, 2007, **3**, 1099–1115.

32 M. Böhmer, *Langmuir*, 1996, **12**, 5747–5750.

33 M. Trau, D. A. Saville and I. A. Aksay, *Science*, 1996, **272**, 706–709.

34 J. J. Juarez, P. P. Mathai, J. A. Liddle and M. A. Bevan, *Lab Chip*, 2012, **12**, 4063–4070.

35 F. Smallenburg, H. R. Vutukuri, A. Imhof, A. van Blaaderen and M. Dijkstra, *J. Phys.: Condens. Matter*, 2012, **24**, 464113.

36 A. Yethiraj and A. van Blaaderen, *Nature*, 2003, **421**, 513–517.

37 K.-Q. Zhang and X. Y. Liu, *Nature*, 2004, **429**, 739–743.

38 M. E. Leunissen, C. G. Christova, A.-P. Hynninen, C. P. Royall, A. I. Campbell, A. Imhof, M. Dijkstra, R. van Roij and A. van Blaaderen, *Nature*, 2005, **437**, 235–240.

39 J. Groenewold and W. K. Kegel, *J. Phys. Chem. B*, 2001, **105**, 11702–11709.

40 H. R. Vutukuri, A. F. Demirçrs, B. Peng, P. D. J. van Oostrum, A. Imhof and A. van Blaaderen, *Angew. Chem., Int. Ed.*, 2012, **51**, 11249–11253.

41 T. Palberg, H. Schweinfurth, T. Köller, H. Müller, H. J. Schöpe and A. Reinmüller, *Eur. Phys. J.: Spec. Top.*, 2013, **222**, 2835–2853.

42 A. van Blaaderen, *MRS Bull.*, 2004, **29**, 85–90.

43 A. van Blaaderen, M. Dijkstra, R. Roij, A. Imhof, M. Kamp, B. W. Kwaadgras, T. Vissers and B. Liu, *Eur. Phys. J.: Spec. Top.*, 2013, **222**, 2895–2909.

44 Y. Y. Diao and X. Y. Liu, *Adv. Funct. Mater.*, 2012, **22**, 1354–1375.

45 Y. Liu, R.-G. Xie and X.-Y. Liu, *Appl. Phys. Lett.*, 2007, **91**, 063105.

46 T. H. Zhang and X. Y. Liu, *Appl. Phys. Lett.*, 2006, **89**, 261914.

47 T. H. Zhang and X. Y. Liu, *J. Phys. Chem. C*, 2007, **111**, 1342–1346.

48 R. Fitzgerald, *Phys. Today*, 2001, **54**, 18–20.

49 W. D. Ristenpart, I. A. Aksay and D. A. Saville, *J. Fluid Mech.*, 2007, **575**, 83–109.

50 J. Morthomas and A. Würger, *Phys. Rev. E: Stat., Nonlinear, Soft Matter Phys.*, 2010, **81**, 051405.

51 W. D. Ristenpart, I. A. Aksay and D. A. Saville, *Phys. Rev. E: Stat., Nonlinear, Soft Matter Phys.*, 2004, **69**, 021405.

52 T. Gong and D. W. M. Marr, *Langmuir*, 2001, **17**, 2301–2304.

53 W. D. Ristenpart, I. A. Aksay and D. A. Saville, *Phys. Rev. Lett.*, 2003, **90**, 128303.

54 F. Nadal, F. Argoul, P. Hanusse, B. Pouligny and A. Ajdari, *Phys. Rev. E: Stat., Nonlinear, Soft Matter Phys.*, 2002, **65**, 061409.

55 W. D. Ristenpart, I. A. Aksay and D. A. Saville, *Langmuir*, 2007, **23**, 4071–4080.

56 K.-Q. Zhang and X. Y. Liu, *J. Chem. Phys.*, 2009, **130**, 184901–184907.

57 X. Y. Liu, *Low Molecular Mass Gelator*, Springer, Berlin, Heidelberg, 2005, vol. 256, pp. 1–37.

58 X. Y. Liu, *AIP Conf. Proc.*, 2007, **916**, 439–465.

59 M. Volmer and A. Weber, *Z. Phys. Chem.*, 1925, **119**, 277–301.

60 R. Becker and W. Döring, *Ann. Phys.*, 1935, **24**, 719–752.

61 J. Frenkel, *J. Chem. Phys.*, 1939, **7**, 538–547.

62 P. Cubillas and M. W. Anderson, in *Zeolites and Catalysis: Synthesis, Reactions and Applications*, ed. J. Čejka, A. Corma and S. Zones, Wiley-VCH Verlag GmbH & Co. KGaA, Weinheim, Germany, 2010, pp. 1–55.

63 J.-L. Li and X.-Y. Liu, *Adv. Funct. Mater.*, 2010, **20**, 3196–3216.

64 X. Y. Liu, in *Perspectives on inorganic, organic, and biological crystal growth: From fundamentals to applications*, ed. M. Skowronski, J. J. DeYoreo and C. Wang, American Institute of Physics, New York, 2007, vol. 916, pp. 439–465.

65 D. Kashchiev, *Nucleation: Basic Theory with Applications*, Butterworth-Heinemann, Oxford, 2000.

66 X. Y. Liu, K. Maiwa and K. Tsukamoto, *J. Chem. Phys.*, 1997, **106**, 1870–1879.

67 M. A. Lovette, A. R. Browning, D. W. Griffin, J. P. Sizemore, R. C. Snyder and M. F. Doherty, *Ind. Eng. Chem. Res.*, 2008, **47**, 9812–9833.

68 A. Saha, J. Lee, S. M. Pancera, M. F. Bräeu, A. Kempter, A. Tripathi and A. Bose, *Langmuir*, 2012, **28**, 11182–11187.

69 H. Oyanagi, Z. H. Sun, Y. Jiang, M. Uehara, H. Nakamura, K. Yamashita, L. Zhang, C. Lee, A. Fukano and H. Maeda, *J. Synchrotron Radiat.*, 2010, **18**, 272–279.

70 E. M. Pouget, P. H. H. Bomans, J. A. C. M. Goos, P. M. Frederik, G. de With and N. A. J. M. Sommerdijk, *Science*, 2009, **323**, 1455–1458.

71 X. Y. Liu, *J. Phys. Chem. B*, 2001, **105**, 11550–11558.

72 L. Farkas, *Z. Phys. Chem.*, 1927, **125**, 236–242.

73 X. Y. Liu, in *Advances in Crystal Growth Research*, ed. K. Sato, K. Nakajima and Y. Furukawa, Elsevier Science, Amsterdam, The Netherlands, 2001, pp. 42–61.

74 A. C. Zettlemoyer, *Nucleation*, Dekker, New York, 1969.

75 X. Y. Liu, in *Nanoscale structure and assembly at solid-fluid interfaces*, ed. X. Y. Liu and J. J. DeYoreo, Springer, London, 2004, vol. I, pp. 109–175.

76 A. S. Mostafa and A. D. Richard, *J. Chem. Phys.*, 1982, **77**, 1517–1526.

77 O. Galkin and P. G. Vekilov, *J. Am. Chem. Soc.*, 2000, **122**, 156–163.

78 J. L. Harland and W. van Megen, *Phys. Rev. E: Stat. Phys., Plasmas, Fluids, Relat. Interdiscip. Top.*, 1997, **55**, 3054–3067.

79 P. Thomas, *J. Phys.: Condens. Matter*, 1999, **11**, R323–R360.

80 O. Galkin and P. G. Vekilov, *Proc. Natl. Acad. Sci. U. S. A.*, 2000, **97**, 6277–6281.

81 P. N. Pusey, in *Liquids, Freezing and the Glass Transition*, ed. J. P. Hansen, D. Levesque and J. Zinn-Justin, North-Holland, Amsterdam, 1991, pp. 763–931.

82 V. M. Fokin and E. D. Zanotto, *J. Non-Cryst. Solids*, 2000, **265**, 105–112.

83 J. W. Schmelzer, A. R. Gokhman and V. M. Fokin, *J. Colloid Interface Sci.*, 2004, **272**, 109–133.

84 T. Kawasaki and H. Tanaka, *Proc. Natl. Acad. Sci. U. S. A.*, 2010, **107**, 14036–14041.

85 A. Stradner, H. Sedgwick, F. Cardinaux, W. C. K. Poon, S. U. Egelhaaf and P. Schurtenberger, *Nature*, 2004, **432**, 492–495.

86 S.-T. Yau and P. G. Vekilov, *J. Am. Chem. Soc.*, 2001, **123**, 1080.

87 J. J. De Yoreo and P. G. Vekilov, in *Biomineralization*, ed. P. M. Dove, S. Weiner and J. J. De Yoreo, Mineralogical Society of America, Washington, D.C., 2003, vol. 54, p. 58.

88 F. Sciortino, P. Tartaglia and E. Zaccarelli, *J. Phys. Chem. B*, 2005, **109**, 21942–21953.

89 P. R. ten Wolde, M. J. Ruiz-Montero and D. Frenkel, *Phys. Rev. Lett.*, 1995, **75**, 2714–2717.

90 J. F. Lutsko and G. Nicolis, *Phys. Rev. Lett.*, 2006, **96**, 046102.

91 A. Navrotsky, *Proc. Natl. Acad. Sci. U. S. A.*, 2004, **101**, 12096–12101.

92 T. H. Zhang and X. Y. Liu, *J. Phys. Chem. B*, 2007, **111**, 14001–14005.

93 E. Beniash, J. Aizenberg, L. Addadi and S. Weiner, *Proc. R. Soc. London, Ser. B*, 1997, **264**, 461.

94 I. M. Weiss, N. Tuross, L. Addadi and S. Weiner, *J. Exp. Zool.*, 2002, **293**, 478.

95 L. Addadi, S. Raz and S. Weiner, *Adv. Mater.*, 2003, **15**, 959.

96 L. Addadi and S. Weiner, *Angew. Chem., Int. Ed. Engl.*, 1992, **31**, 153.

97 S. E. Wolf, I. Lieberwirth, F. Natalio, J.-F. Bardeau, N. Delorme, F. Emmerling, R. Barrea, M. Kappl and F. Marin, *Faraday Discuss.*, 2012, **159**, 433–448.

98 D. Kashchiev, P. G. Vekilov and A. B. Kolomeisky, *J. Chem. Phys.*, 2005, **122**, 244706.

99 T. H. Zhang and X. Y. Liu, *J. Phys. Chem. B*, 2007, **111**, 14001–14005.

100 Y. G. Kuznetsov, A. J. Malkin and A. McPherson, *J. Cryst. Growth*, 2001, **232**, 30–39.

101 W. Ostwald, *Z. Phys. Chem.*, 1897, **22**, 289–330.

102 T. Threlfall, *Org. Process Res. Dev.*, 2003, **7**, 1017–1027.

103 I. N. Stranski and D. Totomanow, *Z. Phys. Chem.*, 1933, **163**, 399–408.

104 J. Baumgartner, A. Dey, P. H. H. Bomans, C. Le Coadou, P. Fratzl, N. A. J. M. Sommerdijk and D. Faivre, *Nat. Mater.*, 2013, **12**, 310–314.

105 X.-Y. Liu, P. Bennema and J. P. van der Eerden, *Nature*, 1992, **356**, 778–780.

106 X.-Y. Liu, P. van Hoof and P. Bennema, *Phys. Rev. Lett.*, 1993, **71**, 109–112.

107 X. Y. Liu, E. S. Boek, W. J. Briels and P. Bennema, *Nature*, 1995, **374**, 342–345.

108 X. Y. Liu and S. W. Lim, *J. Am. Chem. Soc.*, 2003, **125**, 888–895.

109 X. Y. Liu, *Appl. Phys. Lett.*, 2001, **79**, 3539–3541.

110 X. Y. Liu, *J. Chem. Phys.*, 1999, **111**, 1628–1635.

111 X. Y. Liu, *Phys. Rev. B: Condens. Matter Mater. Phys.*, 1999, **60**, 2810–2817.

2346 | *Chem. Soc. Rev.*, 2014, **43**, 2324–2347

This journal is © The Royal Society of Chemistry 2014

112 X. Y. Liu and C. S. Strom, *J. Chem. Phys.*, 2000, **112**, 4408.

113 F. C. Frank, *Discuss. Faraday Soc.*, 1949, **5**, 48–54.

114 R. Ganapathy, M. R. Buckley, S. J. Gerbode and I. Cohen, *Science*, 2010, **327**, 445–448.

115 G. Ehrlich and F. G. Hudda, *J. Chem. Phys.*, 1966, **44**, 1039.

116 R. L. Schwoebel, *J. Appl. Phys.*, 1969, **40**, 614.

117 R. Kunkel, B. Poelsema, L. K. Verheij and G. Comsa, *Phys. Rev. Lett.*, 1990, **65**, 733.

118 K. J. Caspersen, C. R. Stoldt, A. R. Layson, M. C. Bartelt, P. A. Thiel and J. W. Evans, *Phys. Rev. B: Condens. Matter Mater. Phys.*, 2001, **63**, 085401.

119 S. van Dijken, L. C. Jorritsma and B. Poelsema, *Phys. Rev. Lett.*, 1999, **82**, 4038.

120 J. Yu and J. G. Amar, *Phys. Rev. Lett.*, 2002, **89**, 286103.

121 M. Li and J. W. Evans, *Phys. Rev. Lett.*, 2005, **95**, 256101.

122 M. Biehl, in *Multiscale Modeling in Epitaxial Growth*, ed. A. Voigt, Birkhaeuser, Basel, Switzerland, 2005, vol. 149, p. 3.

123 R. Xie and X.-Y. Liu, *J. Am. Chem. Soc.*, 2009, **131**, 4976–4982.

124 X. Y. Liu, in *Selected topics on crystal growth: 14th International Summer School On Crystal Growth*, ed. M. Wang, K. Tsukamoto and D. Wu, American Institute of Physics, Dalian, 2010, pp. 173–220.

125 A. A. Chernov, *Modern Crystallography III - Crystal Growth*, Springer, Berlin, 1984.

126 X. Y. Liu, B. E. P. G. van den Berg, A. R. A. Zauner and P. Bennema, *J. Phys. Chem. B*, 2000, **104**, 11942–11949.

127 J. M. Kosterlitz and D. J. Thouless, *J. Phys. C: Solid State Phys.*, 1973, **6**, 1181–1203.

128 T. Guaratini, M. D. Gianeti and P. M. B. G. M. Campos, *Int. J. Pharm.*, 2006, **327**, 12–16.

129 J. K. Oh, R. Drumright, D. J. Siegwart and K. Matyjaszewski, *Prog. Polym. Sci.*, 2008, **33**, 448–477.

130 A. Vintiloiu and J.-C. Leroux, *J. Controlled Release*, 2008, **125**, 179–192.

131 J. H. Jung, H. Kobayashi, M. Masuda, T. Shimizu and S. Shinkai, *J. Am. Chem. Soc.*, 2001, **123**, 8785–8789.

132 P. Xue, R. Lu, D. Li, M. Jin, C. Tan, C. Bao, Z. Wang and Y. Zhao, *Langmuir*, 2004, **20**, 11234–11239.

133 X. Y. Liu, in *Nanoscale Structure and Assembly at Solid-Fluid Interface*, ed. X. Y. Liu and J. J. De Yoreo, Kluwer Academic Publishers, 2004, vol. 1, p. 109.

134 X. Y. Liu, in *Advances in Crystal Growth Research*, ed. K. Sato, K. Nakajima and Y. Furukawa, Elsevier Science B.V., Amsterdam, 2001, p. 42.

135 X. Y. Liu, *Top. Curr. Chem.*, 2005, **256**, 1–37.

136 A. Hashimoto, K. Suenaga, A. Gloter, K. Urita and S. Iijima, *Nature*, 2004, **430**, 870–873.

137 G.-D. Lee, C. Z. Wang, E. Yoon, N.-M. Hwang, D.-Y. Kim and K. M. Ho, *Phys. Rev. Lett.*, 2005, **95**, 205501.

138 A. Pertsinidis and X. S. Ling, *Phys. Rev. Lett.*, 2001, **87**, 098303.

139 A. Pertsinidis and X. S. Ling, *Nature*, 2001, **413**, 147–150.

140 V. Vitelli, J. B. Lucks and D. R. Nelson, *Proc. Natl. Acad. Sci. U. S. A.*, 2006, **103**, 12323–12328.

141 W. T. M. Irvine, M. J. Bowick and P. M. Chaikin, *Nat. Mater.*, 2012, **11**, 948–951.

142 W. T. M. Irvine, V. Vitelli and P. M. Chaikin, *Nature*, 2010, **468**, 947–951.

143 R. L. Penn and J. F. Banfield, *Science*, 1998, **281**, 969–971.

144 D. Li, M. H. Nielsen, J. R. I. Lee, C. Frandsen, J. F. Banfield and J. J. De Yoreo, *Science*, 2012, **336**, 1014–1018.

145 D. Zhang, P. González-Mozuelos and M. O. de la Cruz, *J. Phys. Chem. C*, 2010, **114**, 3754–3762.